Impact of Al-doped ZnO layer on growth rate and microstructures in polycrystalline Si thin film obtained by Al-induced layer exchange process

Buried Al-doped ZnO (AZO) layer was found to give a drastic impact on Al-induced layer exchange process of amorphous Si (*a*-Si) and Al, and resultant formation of polycrystalline Si thin film. The growth rate of polycrystalline Si was largely enhanced by the presence of AZO through the increased interface roughness between a-Si and Al, which promoted diffusion of Si in Al. Furthermore, a fraction of <100>-oriented crystal grains was found to increase with the presence of AZO.

Realization of wafer-equivalent polycrystalline Si (poly-Si) thin film on large-area low-cost substrates will give a great impact since it could dramatically improve semiconductor devices such as solar cells and flat panel displays. The film should be of high-quality containing large crystal grains with controlled grain orientations and grain boundary characters. Especially, if one could realize <111> or <100>-oriented wafer-equivalent poly-Si thin films, they can be used for subsequent epitaxy of *a*-axis oriented $BaSi_2$ thin films, which could be applied to novel high-efficiency, earth-abundant thin film solar cells [1].

A possible growth method to realize such a high-quality poly-Si thin film is Al-induced layer exchange process (ALILE) of Al and amorphous-Si (*a*-Si) [2]. ALILE starts with stacked structures of a-Si/oxide/Al/substrate followed by annealing below the eutectic temperature (577 °C) in the Al-Si system. After annealing, Al and a-Si layers are exchanged and the initial *a*-Si is transformed into the continuous poly-Si film on the substrate [3-5]. Since ALILE proceeds under near equilibrium conditions with a small amount of supersaturation, the nucleation rate is relatively slow and large crystal grains in the order of 10-100 nm can be obtained. The grain size and the preferential orientation are strongly dependent on the interfacial structures [6] since dissociation of Si atoms in Al proceeds through the a-Si/Al interface. However, controlling mechanisms of microstructures as well as the growth rate have not been fully understood in spite of the importance.

In order to explore these mechanisms, we attempted to modify the interface by using buried aluminum-doped zinc oxide (AZO) to act as the transparent conductive layer and carried out *in-situ* observation of the growth process [7,8]. Glass substrates were cleaned with acetone, methanol, and deionized water. For a part of samples, 650 nm-thick AZO was deposited by radio-frequency magnetron sputtering. The 100 nm-thick Al layers were then deposited using a thermal evaporator. Subsequently, samples were exposed to air for 48 hrs to form the native Al oxide layer followed by deposition of 100 nm-thick a-Si layer. Finally, samples were annealed at 500-550 °C under argon gas ambient. The growth process was monitored in-situ by using a system with a digital optical microscope and a furnace..

Fig. 1 shows snapshots during growth of poly-Si, which indicate surface coverage of Si as a function of the annealing time. The top and bottom images of Fig. 1 express the poly-Si films formed without/with presence of AZO layer. At the same annealing temperature, the crystallization process time of samples with AZO was found to be much shorter than that without AZO. With increasing annealing temperature, the crystallization process time was also rapidly shortened.

One of the possible reasons for the faster growth rate in the sample with AZO is acceleration of the diffusion rate of Si into Al layer. By atomic force microscopy, we have disclosed that the root-mean-square roughness of the glass/Al and glass/AZO/Al layers before annealing was 2.0 and 3.1 nm, respectively. The initial interface roughness affected the

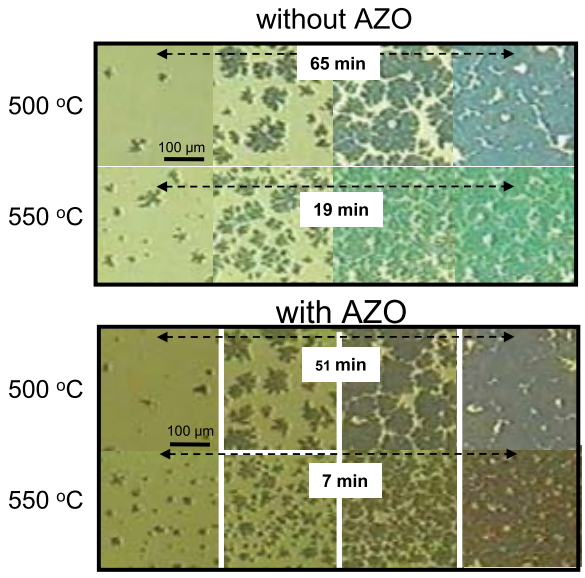

Fig. 1 Snapshots during growth of poly-Si display increase of the Si coverage as a function of annealing time for samples without and with AZO, and different annealing temperatures of 500°C and 550 °C.

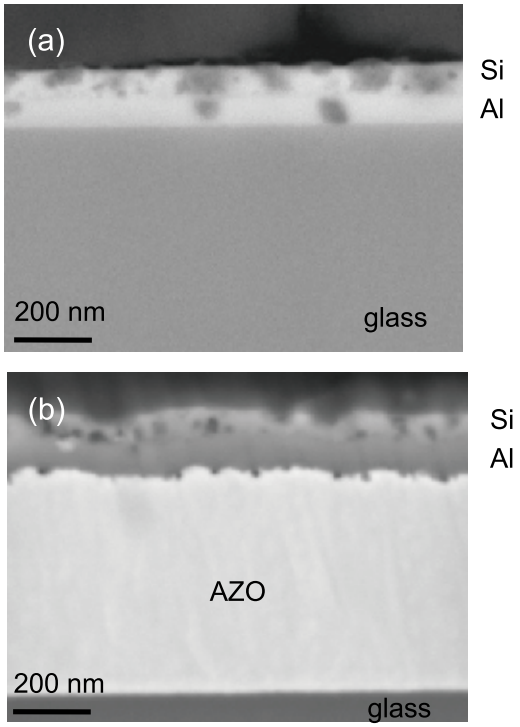

Fig. 2 Cross-sectional scanning electron microscope images of samples (a) without and (b) with AZO after annealing at 500°C

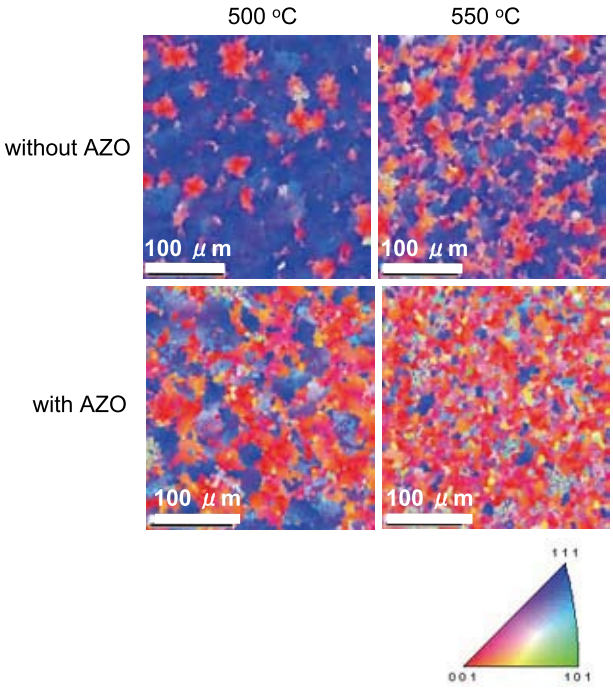

Fig. 3 EBSD crystalline orientation mapping images for poly-Si film

roughness after annealing as shown in Fig. 2. The Al/Si interface of sample without AZO layer is relatively flat and clean, whereas that of sample with AZO layer has a remarkably large roughness. Two-dimensional finite element calculation supported that the increased interface roughness results in the increase in the Si concentration in Al, which enhances the growth rate of poly-Si [8].

Fig. 3 shows the crystalline orientation mapping images for the surface normal direction to poly-Si films. Remarkable variation of crystallographic orientation for each sample was found depending on growth parameters. The presence of the AZO layer and the increase of the annealing temperature were found to lead to increase of <100>-oriented crystal grains. On the other hand, lower annealing temperature was found to result in increase of <111>-oriented crystal grains. Here, we introduce a possible mechanism of the preferential orientation of poly-Si films, which can be determined from the growth rate. Generally, the Si{111} plane with the lowest surface energy tends to have higher stability; however, the Si{100} plane has a higher surface energy with unstable state. In the case of low growth rate, the {111} coverage with lower surface energy is larger than the coverage of other planes. On the other hand, when the growth rate is fast, the {100} coverage with a rough surface is increased. As illustrated by this study, control of the interface can modify ALILE and microstructures in poly-Si thin film [9], which could be a promising route toward realization of wafer-equivalent poly-Si thin film.

References

[1] T. Suemasu and N. Usami, Japanese Patent 2009-115337
[2] G. Majni, and G. Ottaviani, Appl. Phys. Lett. 31, 125 (1977).
[3] O. Nast, T. Puzzer, L. M. Koschier, A. B. Sproul, and S. R. Wenham, Appl. Phys. Lett. 73, 3214 (1998).
[4] A. G. Aberle, N. P. Harder, and S. Oelting, J. Cryst. Growth 226, 209 (2001).
[5] W. Fuhs, S. Gall, B. Rau, M. Schmidt, and J. Schneider, Solar Energy 77, 961 (2004).
[6] M. Kurosawa, N. Kawabata, T. Sadoh, and M. Miyao, Appl. Phys. Lett. 95, 132103 (2009).
[7] M. Jung, A. Okada, T. Saito, T. Suemasu, and N. Usami, Appl. Phys. Express 3, 095803 (2010).
[8] M. Jung, A. Okada, T. Saito, T. Suemasu, C.Y. Chung, Y. Kawazoe, and N. Usami, Jpn. J. Appl. Phys. 50, 04DP02 (2011).
[9] H. Suzuki, N. Usami, A. Nomura, T. Shishido, K. Nakajima, and T. Suemasu, J. Cryst. Growth 312, 3257 (2010)

Keywords: crystal growth, thin films, solar cells
N. Usami (Crystal Physics Division)
E-mail:usa@imr.tohoku.ac.jp
URL:http://www.xtalphys.imr.tohoku.ac.jp

Observation of the Spin Seebeck Effect in Insulators

Spin Seebeck effect (SSE), generation of spin voltage as a result of a temperature gradient, is shown to appear in magnetic insulators, which has been measured only in metals. The observation of the SSE in insulators has been demonstrated in two different configurations. Our findings extend the range of potential materials for thermoelectric applications and provide a crucial piece of information for understanding the physics of the SSE.

For thermoelectric power generation, we often rely on the Seebeck effect, which is the generation of electric voltage as a result of a temperature gradient. In contrast, recent studies on spintronics revealed that a spin analogy for the Seebeck effect, named the spin Seebeck effect (SSE) [1-9], appears in magnets. The SSE stands for the generation of 'spin voltage' as a result of a temperature gradient. Spin voltage refers to the potential for electron's spins, which drives spin currents. The SSE has been reported in several metallic magnets [1], although consensus about its microscopic mechanism has not yet been reached [2].

The conventional Seebeck effect requires itinerant charge carriers, and therefore exists only in electric conductors. It appears natural to assume that the same should hold for the SSE. Here, we show that a magnetic insulator exhibits the SSE despite the absence of conduction electrons (Fig. 1(a)) [3]. This result clearly indicates that thermally induced spin voltage is associated with magnetization dynamics. This new mechanism for the thermo-spin conversion allows us to narrow down scenarios for the physical origin of the SSE.

The observation of the SSE in a magnetic insulator is realized by the inverse spin Hall effect (ISHE) in Pt films [3]. The ISHE enables to convert the spin signal generated by heat flows in the insulator into electric voltage. Fig. 1(b) shows a schematic of the sample used in this study. The sample consists of a single-crystal insulator $LaY_2Fe_5O_{12}$ film with several Pt wires. An external magnetic field H and a temperature gradient were applied along the x direction (Fig. 1(b)). Since the localized magnetic moments in $LaY_2Fe_5O_{12}$ and conduction electrons in Pt are coupled by the interface spin-exchange interaction [10], the SSE in the $LaY_2Fe_5O_{12}$ layer should generate a spin current in the attached Pt layer (Fig. 1(b)). In the Pt layer, the ISHE converts this spin current into an electric field via the spin-orbit interaction. Therefore, we can detect the SSE by measuring electric voltage V between the ends of the Pt wire.

In Fig. 2(a), we show the H dependence of V in the Pt wires, placed at the lower- and higher- temperature ends of the $LaY_2Fe_5O_{12}$ layer, for various values of the temperature

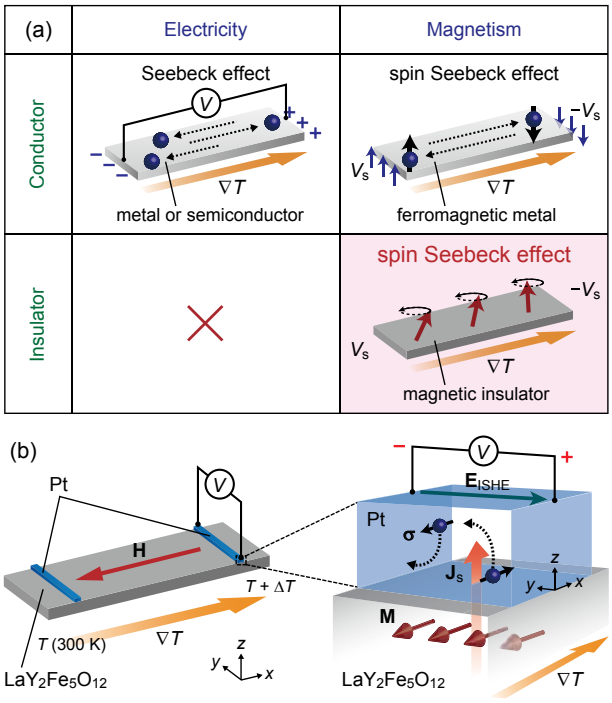

Fig. 1: (a) Seebeck and spin Seebeck effects (SSE). (b) Measurement mechanism for the SSE in an insulator.

difference ΔT. The magnitude of V is observed to be proportional to ΔT in both the setups. The sign of V at finite values of ΔT is clearly reversed between these setups and is also reversed by reversing H; these distinctive behaviors of V are the key features of the SSE [1]. Since the $LaY_2Fe_5O_{12}$ is an insulator, complicating thermoelectric artifacts in itinerant magnets do not exist at all. These results confirm the existence of the spin current injected into the Pt layer which is generated from the temperature gradient in the insulator $LaY_2Fe_5O_{12}$ [3].

Next, we measured the spatial distribution of the thermally induced spin voltage in the same sample structure. Fig. 2(b) shows V as a function of the Pt-wire position for various values of ΔT. When a finite ΔT is applied, V varies linearly along the temperature gradient, similar to the behavior of the SSE in metallic films [1, 3].

We demonstrated the observation of the SSE in a magnetic insulator also in *longitudinal*

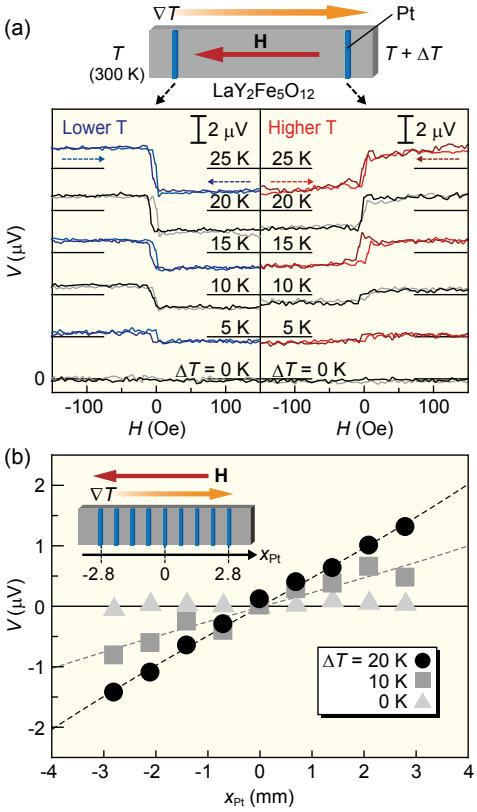

Fig. 2: Magnetic field H dependence (a) Pt-wire-position x_{Pt} dependence (b) of the SSE signal V in the $LaY_2Fe_5O_{12}$/Pt sample.

configuration, in which a spin current is injected *parallel* to a temperature gradient from a ferromagnet into an attached paramagnetic metal [5, 7]. In Fig. 3, we show the experimental results on the longitudinal SSE in an $Y_3Fe_5O_{12}$/Pt system. Since the longitudinal SSE requires only simple and versatile systems, it will extend the range of device application and experimental investigation of the SSE.

The SSE in magnetic insulators can be applied directly to the design of thermo-spin generators and, in combination with the ISHE, thermoelectric generators, allowing new approaches towards the improvement of thermoelectric generation efficiency. In general, the efficiency is improved by suppressing the energy loss due to heat conduction and Joule dissipation, which are realized respectively by reducing the thermal conductivity κ for the sample part where heat currents flow and by reducing the electric resistivity ρ for the part where charge currents flow. However, in electric conductors, the

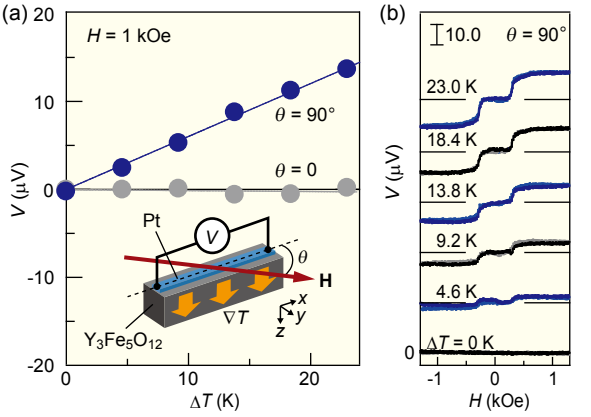

Fig. 3: Temperature-difference ΔT dependence (a) and H dependence (b) of the longitudinal SSE signal V in the $Y_3Fe_5O_{12}$/Pt sample.

Wiedemann-Franz law ($\kappa\rho$~constant) limits this improvement. In contrast, in the present SSE setups, κ and ρ are independent since the heat and charge currents flow in different parts of the sample [3, 5, 7]. The thermoelectric generation efficiency of our SSE devices is still small, but can be enhanced by reducing the phonon contribution to the thermal conductivity of the insulator layer and by improving the interface spin-exchange efficiency.

References

[1] K. Uchida, S. Takahashi, K. Harii, J. Ieda, W. Koshibae, K. Ando, S. Maekawa, and E. Saitoh, Nature **455** (2008) 778.
[2] J. Xiao, G. E. W. Bauer, K. Uchida, E. Saitoh, and S. Maekawa, Phys. Rev. B **81** (2010) 214418.
[3] K. Uchida, J. Xiao, H. Adachi, J. Ohe, S. Takahashi, J. Ieda, T. Ota, Y. Kajiwara, H. Umezawa, H. Kawai, G. E. W. Bauer, S. Maekawa, and E. Saitoh, Nature Mater. **9** (2010) 894.
[4] C. M. Jaworski, J. Yang, S. Mack, D. D. Awschalom, J. P. Heremans, and R. C. Myers, Nature Mater. **9** (2010) 898.
[5] K. Uchida, H. Adachi, T. Ota, H. Nakayama, S. Maekawa, and E. Saitoh, Appl. Phys. Lett. **97** (2010) 172505.
[6] H. Adachi, K. Uchida, E. Saitoh, J. Ohe, S. Takahashi, and S. Maekawa, Appl. Phys. Lett. **97** (2010) 252506.
[7] K. Uchida, T. Nonaka, T. Ota, and E. Saitoh, Appl. Phys. Lett. **97** (2010) 262504.
[8] C. M. Jaworski, J. Yang, S. Mack, D. D. Awschalom, R. C. Myers, and J. P. Heremans, Phys. Rev. Lett. **106** (2011) 186601.
[9] K. Uchida, H. Adachi, T. An, T. Ota, M. Toda, B. Hillebrands, S. Maekawa, and E. Saitoh, Nature Mater. (in press).
[10] Y. Kajiwara, K. Harii, S. Takahashi, J. Ohe, K. Uchida, M. Mizuguchi, H. Umezawa, H. Kawai, K. Ando, K. Takanashi, S. Maekawa, and E. Saitoh, Nature **464** (2010) 262.

Keywords: spintronic, spin current, thermoelectricity
K. Uchida and E. Saitoh (Materials Property Division)
E-mail: saitoheiji@imr.tohoku.ac.jp
URL: http://saitoh.imr.tohoku.ac.jp/

Advance and Recent Activity of Neutron Group of IMR

IMR is a unique institute even in the world which has a neutron facility based on the strong background of advanced material science. IMR neutron scattering group is investigating issues in materials science, such as ferroelectric materials, high-Tc superconductivity, as well as developing high performance devices in neutron science. In particular, the group is aiming at constructing an originative neutron spectrometer with oncoming-generation technologies in J-PARC, which will be a flagship instrument of material science in IMR.

1) Advanced Spectrometer Project

(K. Ohoyama)

Metal Physics with Quantum Beam Spectroscopy group (Yamada Lab.) and Center of Neutron Science for Advanced Materials are advancing a project to construct a world top class spectrometer at the brightest neutron beam facility of Japan Proton Accelerator Research Complex (J-PARC), based on collaborations with KEK (project leader: K. Ohoyama) (Fig.1).

The spectrometer is characterised by polarised neutrons, which are very sensitive to observe pure magnetic correlations. Since there exist just a few polarised neutron spectrometers in the world, this spectrometer will be a key instrument to generate breakthroughs in novel material science in Japan. In 2010, the project team succeeded in preliminary polarised neutron experiments, using a ^{3}He gas type neutron spin polarisers developed by collaborations with KEK, JAEA and IMR. Now, the spin polariser/analyser for this project is in the progress of production. Moreover, we have estimated performances of the spectrometer, such as flux, resolution, and polarisation, based on test measurements on IMR neutron instruments, and Monte Carlo simulation. By optimization of designs, satisfactory performance have been obtained; the polarised neutron flux of the spectrometer is expected to be 1.1E+5 (n/s/cm^2/meV) at 100meV, and the neutron polarisation to be ~90%.

To make this spectrometer originative in the world, we have been developing an epoch-making technology: the cross correlation method, which will give drastic improvement of efficiency and S/N ratio of measurements of spectroscopy.

In 2011, this project succeeded in gaining authorisation by J-PARC Center. Aiming at beginning the construction from 2012, detailed engineering designs have already begun.

2) Mechanism of Relaxor Ferroelectrics

(M. Matsuura)

Ferroelectric materials are widely used in our daily life, such as condensers in cellular phone, computer, etc., almost all electric devices. Relaxor ferroelectrics have gained huge attention from industrial and scientific points of view, because they show extremely high dielectric susceptibility and piezoelectric responses over a wide temperature range[1] which enable thinner and smaller condensers with the same quality.

In relaxor ferroelectrics, it is known that randomly oriented polar nanoregions (PNRs) are formed from high temperatures[2], as shown schematically in Fig.2a, and play an important role in the giant dielectric response and its thermal evolution. From inelastic neutron scattering studies on a single crystal of relaxor ferroelectric $0.7Pb(Mg_{1/3}Nb_{2/3})O_3$-$0.3PbTiO_3$, we have clarified that flipping motion of electric dipoles (relaxation) in PNRs are coupled with lattice vibrations (phonon) in surrounding regions[3], as schematically shown in Fig. 2b. Through the mode-coupling between phonon and relaxation modes, some regions

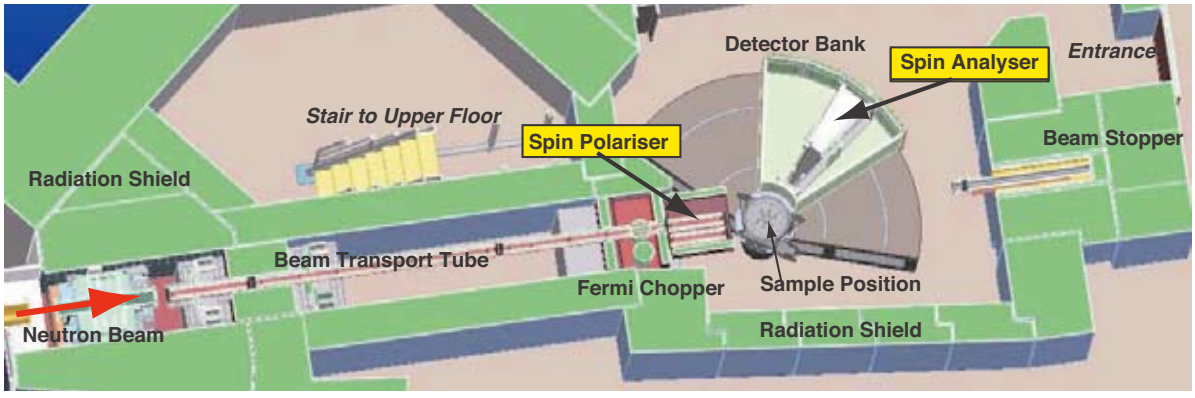

Fig. 1 A rendering view of the spectrometer of the collaboration project of Tohoku Univ. and KEK.

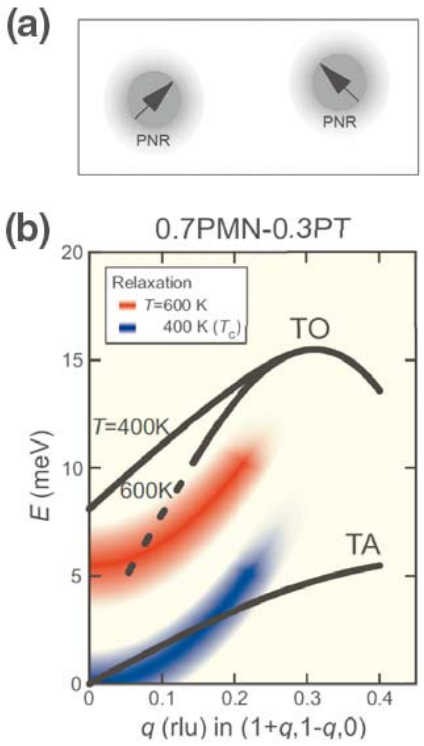

Fig.2: (a) Schematic diagram of polar nanoregion (PNR). Arrows indicate direction of electric dipoles in PNRs. (b) Schematic diagram of transverse acoustic (TA) and soft transverse optical (TO) phonon dispersion curves in relaxor $0.7Pb(Mg_{1/3}Nb_{2/3})O_3$-$0.3PbTiO_3$ (0.7PMN-0.3PT). The gradated thick lines indicate the *q*-dependence of the relaxation frequency at *T*=600K (red) and 400K (blue). [3]

surrounding PNRs become polar by atomic shift along an electric dipole of each PNR from ideal cubic positions, which leads to enlargement of PNRs. The new growth mechanism of PNRs not only explains the relaxor properties over a wide temperature range but also unifies different approaches based on order-disorder-type and displacive-type lattice dynamics.

3) Development of Novel Neutron Devices

(H. Hiraka)

A development of neutron monochromator is one of the instrumental key issues in neutron science. Stimulated by recent development in plastically deforming techniques for Si-crystal wafers by Nakajima *et al.* [4], we explored its potential of a deformed-wafer crystal for a novel neutron monohromator or analyzer crystal.

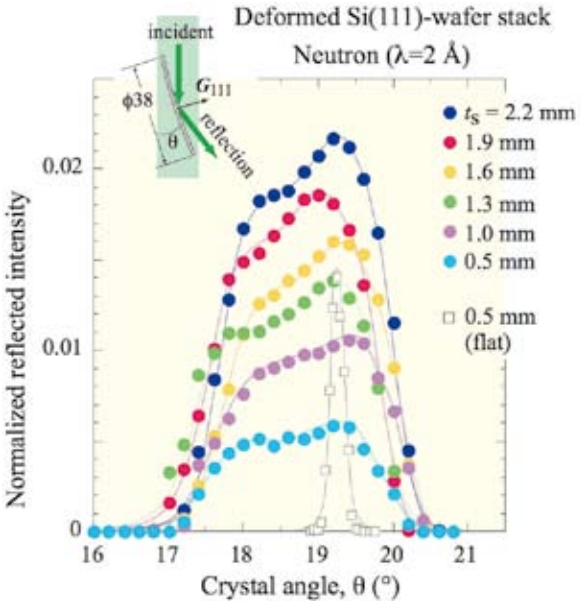

Fig. 3. Rocking curves of (111) Bragg reflection using deformed Si wafers with *R*=600 mm. The reflected intensity is normalized by the direct-beam intensity. For reference, a resolution-limit Bragg reflection of a flat wafer is also plotted by open squares. The lines are drawn as a guide to eyes.

Fig. 3 shows that the angle-integrated intensity is amplified by a factor of ~4 for the 0.5-mm wafer during the deformation process[5]. Moreover, the scattered intensity successively increases as the thickness of the deformed-wafer stack (*ts*) increases. Therefore, further stacking can provide a way of increasing reflected neutrons more. Besides, this plastic deformation has a pronounced advantage in forming an intense curvature, unlike mechanically (or elastically) bent crystals. We are planning to equip these unique wafers for neutron analyzer elements because a relatively wide-angle divergence of neutron beam is acceptable for a detector. We have taken out a patent on this technique[6].

References

[1] S.-E. Park and T. R. Shrout: J. Appl. Phys. **82** (1997) 1804.
[2] G. Burns and F. H. Dacol: Solid State Commun. **48** (1983) 853.
[3] M. Matsuura *et al.*, submitted to JPSJ
[4] K. Nakajima *et al.*, Nat. Mater. **4** (2005) 47.
[5] H. Hiraka *et al.*, Nucl. Instr. And Meth. **A 635**(2011)137.
[6] H. Hiraka *et al.* Japan patent 2009-066185.

Keywords: J-PARC spectrometer project, relaxor ferroelectrics, novel neutron devices
K.Yamada, K.Ohoyama, H. Hiraka, M. Matsuura, T. Sato, and J. Sungdae (Metal Physics with Quantum Beam Spectroscopy)
URL: http://www.yamada-lab.imr.tohoku.ac.jp/jp/index.html

Microstructure Changes in Nuclear Reactor Pressure Vessel Steels by Neutron Irradiation and their Effects on Mechanical Properties

Understanding of the embrittlement mechanism of nuclear reactor pressure vessel (RPV) steels by neutron irradiation is one of the most important subjects for safety operation of nuclear power plants. Here, we investigate the correlation of microstructure evolution and hardening in RPV steels irradiated in a material testing reactor. Three-dimensional atom probe and positron annihilation are used to clarify the contributions of solute nano-clusters and matrix damages to the irradiation hardening. Irradiation-induced changes of the atomic distributions of solute and impurity elements around carbides were also revealed.

The irradiation-induced embrittlement of the nuclear reactor pressure vessel (RPV) steels is currently a vital issue for ensuring the safe operation of nuclear power plants. The embrittlement is considered to be mainly caused by the irradiation-induced changes in the microstructure such as the formation of the solute nano-clusters (SCs) and matrix damages (MDs) due to irradiation-induced point defect clusters and dislocation loops. However, in spite of the extensive studies, the details of the microstructural changes and their effects on the mechanical properties are not well clarified.

One of the reasons is due to the difficulty in the observation of the microstructural changes even by state-of-the-art transmission electron microscopy. In this study, we overcome the difficulty by employing three-dimensional atom probe (3DAP) and positron annihilation (PA). 3DAP, which can map out the alloying elements in three-dimensional space with near-atomic resolution, enables us to reveal the detail morphology of the SCs. However, 3DAP gives us no information about MDs. On this issue, PA technique is a powerful tool for vacancy-related MDs. Here, we investigate the correlation of microstructure evolution and hardening in the RPV steels by neutron irradiation using 3DAP and PA to clarify the contributions of SCs and MDs to the irradiation hardening.

The samples are A533B type steels with high Cu concentration (0.16wt.%) irradiated in the JMTR (Japan Materials Testing Reactor) in the wide range of doses (0.32 - 9.9 × 10^{19} n cm^{-2}) under almost the same flux (1.6-1.9 × 10^{13} n cm^{-2} s^{-1}) at 290 °C. Fig. 1 shows the dose dependence of irradiation hardening (variation of Vickers microhardness). Rapid hardening at low doses below 1 × 10^{19} n cm^{-2} and gradual hardening with further increasing irradiation dose are exhibited.

Typical elemental maps of solute atoms in the samples subjected to different doses obtained by 3DAP are shown in Fig. 2 [1]. These maps reveal approximately spherical Cu rich (Mn, Ni, Si cosegregated) SCs with about 1-2 nm radius. We can estimate the contribution to the hardening due to the SCs based on Russell-Brown model [2] using the obtained 3DAP data (sizes and volume fraction of the SCs). The results are shown in Fig. 1, suggesting that the SCs formation is responsible for the origin of the gradual hardening above 1 × 10^{19} n cm^{-2}, while the initial rapid hardening below 1 × 10^{19} n cm^{-2} could be due to the other origin: *i.e.* MDs. This claim is strongly supported by PA experiments because the positron lifetime rapidly increases with the dose below 1 × 10^{19} n cm^{-2}, due to the positron trapping at MDs [1].

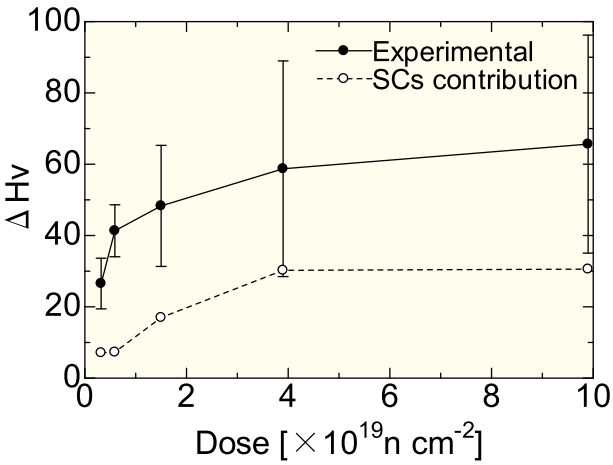

Fig. 1: Dose dependence of irradiation hardening for A533B steels. Estimated SC contribution for the hardening using 3DAP data based on Russell-Brown model [2] is also shown.

We have also studied irradiation-induced microstructural changes of the atomic distributions of solute and impurity elements around carbides in a RPV steel, a surveillance test specimen of Doel-4 reactor in Belgium, using 3DAP [3]. Fig. 3 shows the elemental maps of solute atoms around the carbide in the unirradiated specimen. Nano-scale Fe-Mn-Cr-Mo carbides (~M_6C type) are observed. Mn, Cr and Mo were enriched around the inner carbide-matrix interface. The depletion of Si in

the carbide and the segregation of P at the interface are also observed.

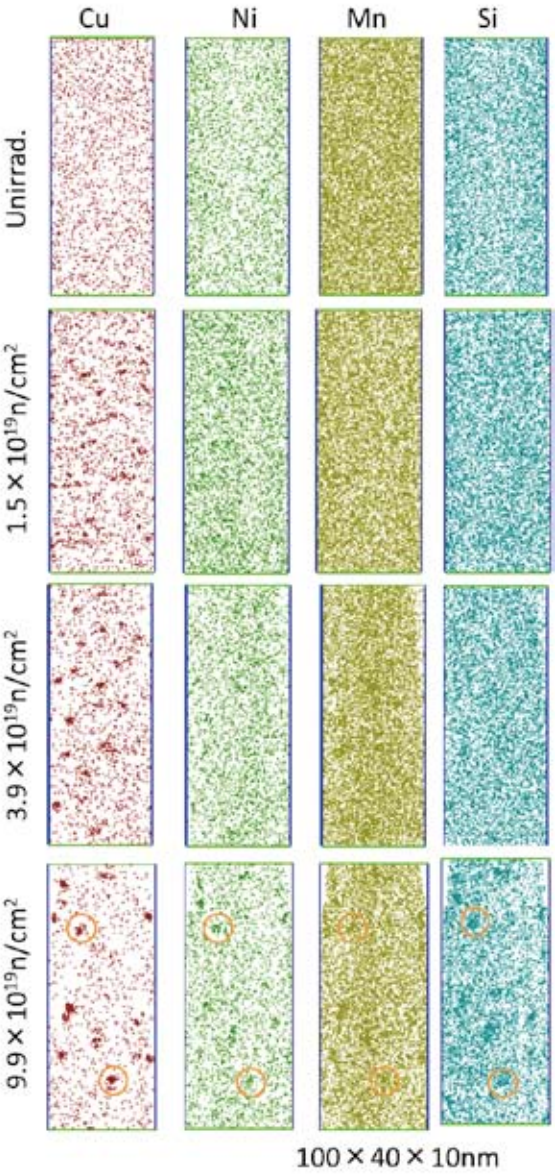

Fig. 2: Elemental maps of Cu, Ni, Mn and Si atoms in A533B type steels neutron-irradiated with various doses.

By neutron irradiation for 12 years, the Mn concentration within the carbide is increased and the enhancement of Mn, Cr and Mo concentration around the carbide- matrix interface as well as P segregation at the interface are markedly intensified [3].

These changes could be one of the possibilities for degradation of the interface, which would contribute to the embrittlement of RPV steels.

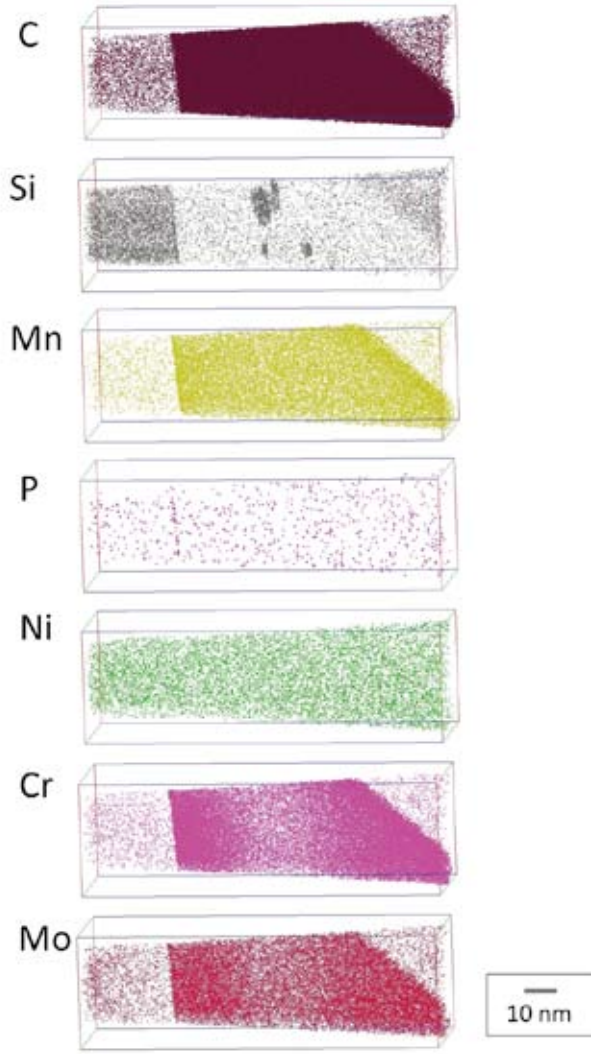

Fig. 3: Elemental maps of C, Si, Mn, P, Ni, Cr and Mo atoms around the carbide in the unirradiated Doel-4 specimen.

References

[1] T. Takeuchi, A. Kuramoto, J. Kameda, T. Toyama, Y. Nagai, M. Hasegawa, T. Ohkubo, T. Yoshiie, Y. Nishiyama and K. Onizawa, J. Nucl. Mater. 402, 93 (2010)
[2] K.C. Russell, L.M. Brown, Acta. Metall. 20, 969 (1972)
[3] T. Toyama, N. Tsuchiya, Y. Nagai, A. Almazouzi, M. Hatakeyama, M. Hasegawa, T. Ohkubo, E. van Walle, R. Gerard, J. Nucl. Mater. 405, 177 (2010)

Keywords: neutron irradiation, embrittlement, atom probe tomography
Y. Nagai (Irradiation Effects in Nuclear and Their Related Materials)
E-mail: nagai@imr.tohoku.ac.jp
URL: http://wani.imr.tohoku.ac.jp
Category: Energy-related Materials

Ion-induced Luminescence and its Application to Analysis of Dynamic Damage Process

Irradiation induced luminescence was used to investigate dynamic process of damage accumulation in dielectric materials. The evolution curves of the luminescence intensity during the H and He ion bombardment were analyzed to examine the defect production and annihilation process caused by the nuclear collisions and electronic excitation.

Drastic changes in the structural and electrical properties of dielectric materials under irradiation are of great interest for their application to fission and fusion devices [1].

Electronic excitation processes play important roles for creating defects in ceramics, known as color centers and excitons in ionic crystals and oxides. Those radiation induced phenomena such as optical absorption and radio-luminescence can be potentially powerful tools capable of examining modification and its evolution under irradiation condition. For example, in silica glasses, we have been successfully investigated neutral oxygen deficiency centers (ODCs), which are not able to be detected by a probe sensitive to paramagnetic defects such as E'centers, the peroxy radicaland non-bridging oxygen hole center (NBOHC), by using the ion-induced luminescence methods [2-4]. An advantage of the ion-beam induced luminescence is that conventional ion-beam analysis techniques are simultaneously applicable to obtain compositional depth distribution of lattice atoms and displaced atoms up to several μm. The combined techniques were used to investigate the interaction between hydrogen and irradiation induced damages in tritium breeding ceramics [5, 6], and? tungsten oxides[8-10]. Recently, we are trying to apply the ion-induced luminescence to polymer films[10-12], to search a possibility of constructing a tow-dimensional monitoring system for the ionizing radiation.

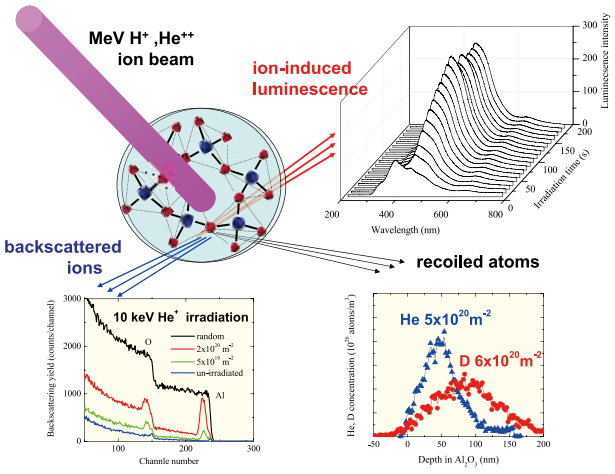

Fig.1: A Schematic illustration of an in-situ measurement of ion–induced luminescence combined with ion-beam analysis techniques.

In the experiment, the evolution of the ion-induced luminescence spectrum is obtained under the irradiation with MeV energy light ions such as H and He ions. Simultaneously, back-scattered and forward-recoiled particles from samples are detected to evaluate variation of atomic composition in the near surface layer, as schematically shown in Fig. 1. In silica glasses, we observed three broad peaks of ion-induced luminescence, originated from NBOHC, ODCII(B2α) and ODCII(B2β) centered at around 1.9, 2.7 and 3.1 eV, respectively. The B2βband immediately diminished at a very small ion fluence, and the B2α band started to increase with successive irradiation, depending on its OH content. The higher intensity of ODCII(B2α) in the lower-OH silica may be explained by a speculation that the glass network was more strained in low-OH silica, where Si-O-Si bonds are easily broken into oxygen deficiency centers to stabilize the glass network. The 1 MeV H and He ion induced luminescence from a synthesized silica glass containing 800 wt.ppm OH plotted as a function of incident ion fluence. The ODCII(B2α) emission intensity increased from zero with an increase of the ion fluence, and tended to saturate at higher fluence. Assuming a first order reaction for the increase of the luminescence intensity under the local energy deposition along the ion trajectory, the formation and annihilation rates of the luminescence centers can be estimated from the evolution curves as shown in Fig. 2. The production rates by H ion irradiation, however, are lower than the annihilation rates, indicating that the annihilation by H ion irradiation is more prominent in comparison with He ion irradiation. This result was reasonably explained by the relation between the nuclear stopping and electronic stopping for the different ions and energies.

Ion bombardment of the polymer materials, in particular, causes important chemical transformations, depending on the energy deposition mechanisms. An aromatic polymer similar to polyethylene terephthalate (PET) is polyethylene naphthalate (PEN), consisting of two benzene rings in a monomeric structure. Both films exhibited characteristic

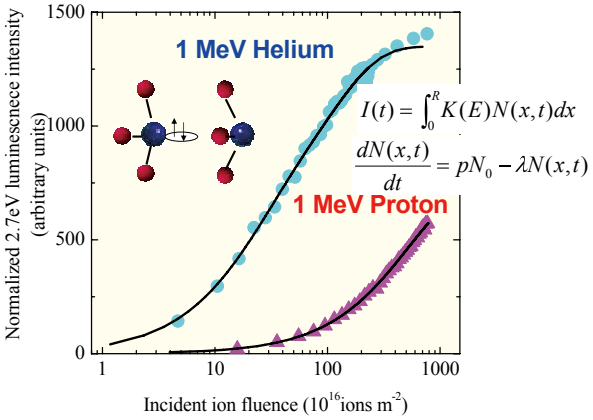

Fig. 2: Evolution of the luminescence intensity under 1 MeV H and He ionirradiation plotted as a function of incident ion fluence. Inserted solid curves are fitted by a model with parameters of production and annihilation rate constants.

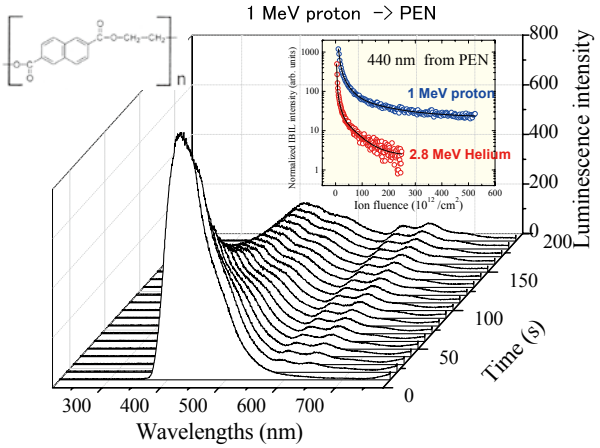

Fig. 3: Ion induced luminescence spectra from a PEN film under 1MeV H ion bombardment plotted as a function if irradiation time. The inserted graph shows the Evolution of the luminescence intensity at 440 nm from the PEN film irradiated by1 MeV H+ and 2. 8 MeV He++ ions.

luminescence bands mainly in the blue region and the luminescence intensity monotonically decreased with ion fluence. According to the simultaneous Fourier-transform infrared absorption measurements, the CH_2 bending vibration of the trans-configuration of the ethylene glycol residue and typical vibration bands of the para-substituted benzene rings were assigned to the bands at 1471 and 1504 cm^{-1}, respectively. The absorption due to these bands gradually decreased with increasing incident ion fluence, suggesting the loss of crystallinity and the scission of the main chain at the para position. The ratio of the damaged cross-sections of H to He is comparable for the PET and PEN films, suggesting that the damage processes of the luminescence centers in both films are essentially the same. On the other hand, the ratios of the stopping power of H to He are considerably smaller in both films. The luminescence centers along the H^+ ion trajectories effectively damaged, and an excess of the energy was deposited around the He^+ ion trajectory for altering the luminescent structure. The back-scattering and Forward-scattering analysis revealed that H, C, and especially O were lost during the ion irradiation. An Al coating of about 100 nm was successfully applied to reduce the degradation of the PET and PEN films. The suppression of the loss of elements from the films indicated that the thin Al layer works as a barrier for volatile molecules caused by local heating and charging effects by incident ions.

References

[1] T. Shikama, K. Toh, S. Nagata, B. Tsuchiya, M. Yamauchi, T. Nishitani, T. Suzuki, K. Okamoto, N. Kubo, *Nuclear Fusion* **46**, 46(2006).
[2] S. Nagata S. Yamamoto, K. Toh, B. Tsuchiya, N. Ohtsu, T. Shikama, H. Naramoto, *J. Nucl. Mater.* **329**,1507(2004) .
[3]M. Watanabe, T. Yoshida, T. Tanabe, S. Muto, A, Inouye, S. Nagata, *Nucl. Instrum.and Meth.B* **250**, 174 (2006)
[4] S. Nagata, H. Katsui, B. Tsuchiya, A. Inouye, S. Yamamoto, K. Toh, T. Shikma, *J. Nucl. Mater.* **367**, 1009 (2007).
[5] H. Katsui, S. Nagata, K. Toh, B. Tsuchiya, T. Shikama, *J. Nucl. Mater.* **386**, 1074 (2009).
[6] H. Katsui , S. Nagata, B. Tsuchiya, T. Shikama., *Nucl. Instrum. and Meth. B* **268**, 2735 (2010).
[7] S. Nagata, A. Inouye, S. Yamamoto, B. Tsuchiya, K. Takano, K. Toh, T. Shikamaet., *J. Alloys and Comp.* **446**, 558 (2007).
[8] A. Inouye, S. Yamamoto, S. Nagata, M. Yoshikawa, T. Shikama, *Nucl. Instr. and Meth. B* **267**, 1480 (2009).
[9] S. Nagata, H. Fujita, A. Inouye, S. Yamamoto, B. Tsuchiya, T. Shikama., *Nucl. Instrum. and Meth. B* **268**, 3099(2010)
[10]S. Nagata, K. Takahiro, B. Tsuchiya, H. Katsui, T. Shikama, *Nucl. Instrum. and Meth .B* **267**, 1553 (2009).
[11] S. Nagata, H. Katsui, K. Takahiro, B. Tsuchiya, T. Shikama, *Nucl. Instrum. and Meth. B* **268,** 3099(2010)
[12]M.Saito, F.Nishiyama, K.Kobayashi, S.Nagata, K. Takahiro, *Nucl. Instrum. and Meth. B* **268,** 2918(2010)

Keywords: luminescence, ion-solid interactions, nuclear material
T.Shikama S.Nagata and M.Zhao (Nuclear Materials Science)
E-mail:nagata@imr.tohoku.ac.jp
URL:http:// www-lab.imr.tohoku.ac.jp/~wshikama/

Effects of Displacive Radiations and Hydrogenation in Zr- and Fe-based Alloys Investigated by Ion-accelerator, HVEM and Nano-hardness

To develop materials for advanced light water reactors and fusion reactors, we investigated Zr- and Fe-based alloys by means of ion irradiation, HVEM and nano-hardness. Hardening of Zr-Nb alloys was evident at less than 1 dpa (displacement per atom) followed by saturation whose value depends on composition. In Fe-alloy we have found that one-dimensional motion of defect clusters which have been noticed in high purity iron and FCC metals. Effect of helium upon irradiation hardening was observed even at relatively lower doses in F82H.

The mechanical degradations of nuclear materials strongly depend on their environments. For instance, Zr-alloys for cladding in LWRs are affected by distribution of hydrides as well as irradiation defects, and Fe-alloy for fusion blanket is done both by radiations and helium accumulation. Therefore, it is indispensable to understand the microstructural evolutions and resulting mechanical degradations and to clarify their correlations. We investigate hardening induced by ion irradiation and/or He/H implantation in Zr- and Fe-based alloys by nano-hardness tester, electron microscopy, as well as fundamental study on stability of defect clusters under electron irradiation in HVEM.

(1) Effects of ion irradiation in Zr-Nb alloys

Zr-1.8Nb (J1), Zr-1.6Nb-0.1Cr (J2) and Zr-2.5Nb (J3) (in mass %) were subjected to ion irradiation, followed by nano-hardness measurement. Irradiations with 4 MeV Ni^{3+} ions to the dose up to 11 dpa (displacement per atom) at 573K were performed at HIT facility, University of Tokyo. Fig. 1 shows dose dependence of irradiation hardening [1]. The steep increase at the early stage of irradiation followed by saturation roughly above 1 dpa was evident. The level of saturation depended on materials, and the effect of solution, Cr, presumably resulted in reducing irradiation hardening. In this study, we investigate effect of hydrogenation in the alloys which will be described elsewhere [2].

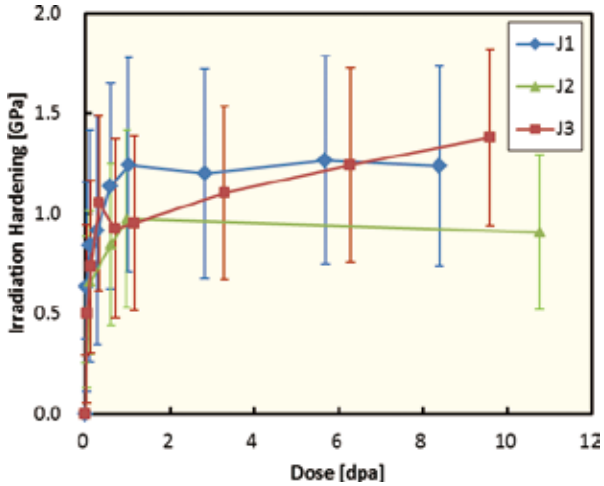

Fig. 1 Irradiation hardening in Zr-Nb alloys under irradiation with 4MeV Ni^{3+} ions at 573K.

(2) Motion of defect clusters in Fe-alloy

Recent theoretical and experimental studies have confirmed that small interstitial clusters in pure metals cause a gliding motion along the direction of the Burgers vector with low activation energy, called one-dimensional (1D) migration [3]. This phenomenon has been suggested to affect defect structural development under irradiation with high-energy particles, such as void swelling. Although 1D migration processes in practical alloys have

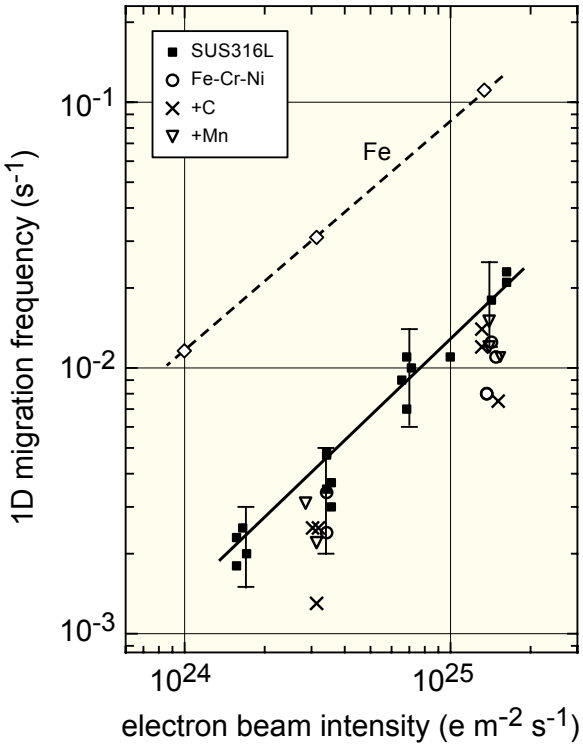

Fig. 2. Frequency of 1D migration of interstitial clusters in SUS316L and its model alloys as a function of electron beam intensity.

technical and fundamental significance for developing materials for nuclear power applications, they are not well understood. In the present study, 1D migration of interstitial clusters in austenitic stainless steel SUS316L and its model alloys, namely, Fe-18Cr-13Ni, Fe-18Cr-13Ni-0.012C, and Fe-18Cr-13Ni-1.7Mn, was examined using in-situ observation by high-voltage electron microscopy. As shown in Fig. 2, such 1D migration was confirmed to occur along the <110> direction at irregular intervals in all these alloys under 1250 kV electron irradiation at room temperature. The frequency of 1D migration was found proportional to electron beam intensity, and was about 1/10 that in high-purity iron under the same irradiation intensity. The distance of 1D migration in the four alloys was less than 10 nm, which was much shorter than that in high-purity iron. No clear difference in the frequency or distance of 1D migration was observed among the four alloys, suggesting that minor solute/impurity elements have no apparent effect on 1D migration in SUS316L.

(3) Irradiation and He-induced hardening in RAFM steel

Reduced activation ferritic/martensitic (RAFM) steel has been recognized as a primary near-term candidate material for nuclear fusion reactors [4]. In the fusion reactor environment, irradiation of 14 MeV neutrons might produce a large amount of displacement damage and transmutant helium (He) atoms in structural materials. For example, 100 dpa of displacement damage and 1000 appm of helium concentration will be raised to RAFM steel after 10 MW/m^2 of neutron wall loading [5].

In the previous research [5,6], ion-irradiated F82H steel to high He/dpa at 633 K caused the radiation hardening accompanied by the formation of black dot defects, which were probably dislocation loops, radiation induced precipitates and nano-voids. Under neutron irradiation, the radiation hardening caused by irradiation- induced dislocation loops and precipitates changes occurred at irradiation temperatures up to 693 K.

The present work investigated the irradiation hardening behaviors and the mechanisms in single and dual ion irradiated F82H steel by combining multi-ion irradiation, ultra-micro-indentation technique and microstructural evolution. F82H steel (IEA-heat) was irradiated in various conditions with single/dual ion beam at the HIT facility. For the single ion irradiation experimental, 4 MeV Ni^{3+}, 2.8 MeV Fe^{2+} and 1 MeV O^+ ions were induced at 573 K, and 2.8 MeV Fe^{2+} and 1 MeV He^+ ions were induced for dual ion irradiation test at the same conditions. And nano-hardness test was performed followed by microstructural observation in order to evaluate and identify the irradiation hardening behavior as shown in Fig. 3.

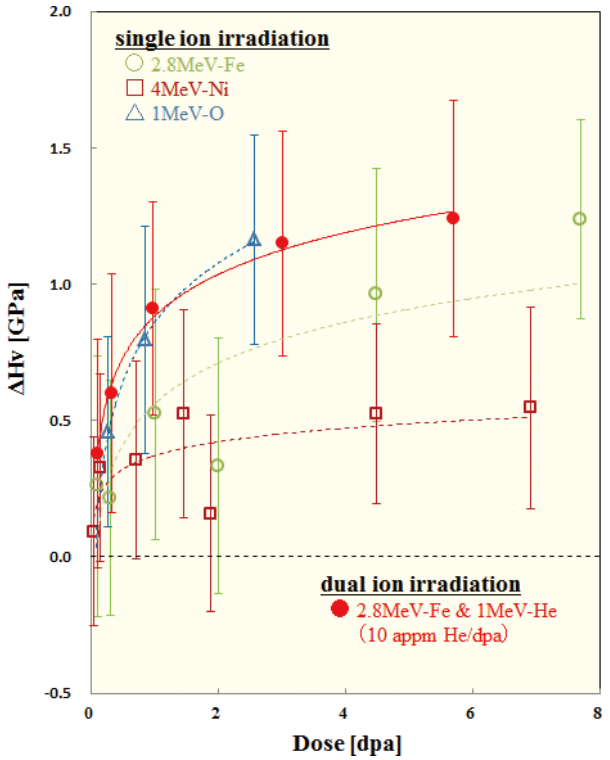

Fig. 3 Irradiation hardening behavior by single and dual ion irradiation at 573K for F82H steel.

References

[1] Y. Satoh et al, Philos. Mag. 89 (2009) 1489.
[2] K. Shiba et al., J. Nucl. Mater. 329–333 (2004) 243.
[3] M. Ando et al., J. Nucl. Mater. 329–333 (2004) 1137.
[4] H. Ogiwara et al., J. Nucl. Mater. 367-370 (2007) 428.

Keywords: ion irradiation, electron irradiation, mechanical properties, electron microscopy
Hiroaki ABE (Nuclear Materials Engineering)
E-mail: abe.hiroaki@imr.tohoku.ac.jp
URL: http://www-lab.imr.tohoku.ac.jp/~abeken/

New Approach for Designing Mg Based BMG Matrix Composite with in-situ α-Ti Dispersoids

A $Mg_{61}Cu_{28}Gd_{11}$ BMG matrix composite with in-situ α-Ti dispersoids was successfully synthesized by mixing a prealloy comprising Ti_2Cu and Cu-Gd compounds and pure Mg melt followed by copper-mold casting. The Cu-Gd phases along with just the Cu from the Ti_2Cu phase were selectively dissolved into the Mg melt to form $Mg_{61}Cu_{28}Gd_{11}$ bulk metallic glass former, and the remaining Ti formed porous structures that were dispersed in the melt. The size of the in-situ α-Ti dispersoids is directly related to that of the Ti_2Cu in the prealloy, and is thus controllable by the cooling rate used in the prealloy preparation. The maximum fracture stress in four-point bending mode was increased from 230 MPa to 387 MPa upon refining the α-Ti dispersoids. The relationship for improving tensile properties, $L \approx R_p$, where L is the size of the porous α-Ti and R_p is the size of the process zone, was achieved.

Mg-based bulk metallic glass (BMG) is a promising structural material because of its high specific strength (~2.3×10^5 Nm/kg) despite the low fracture toughness (a few MPa $m^{1/2}$) as low as that of brittle ceramics [1]. To amend this low toughness, many efforts have been made to develop Mg-based BMG matrix composites (BMGMC) [2-5]. The mechanical property assessment of the composites reported in those works, however, was mostly performed under compressive mode instead of the tensile one.

A composite with in-situ precipitates bonded strongly with the matrix has become a particular interest because they have clean oxide-free surfaces. In addition, these precipitates tend to have higher aspect-ratio shapes, i.e. dendritic, ellipsoidal or flaky, which are effective for bridging any separation of BMG at the shear planes under tension. Accordingly, we developed Mg-based BMG composite containing the in-situ precipitation of α-Ti to improve the tensile property. The alloy design was based on the formula which effectively enhances tensile plasticity of the BMGMC [6], i.e. $L \approx S \approx R_p$, where L is the dendrite size, S is the inter-dendrite spacing and R_p is the length scales of the process zone. Because of the small R_p may lead to the very low toughness of Mg-based BMG, the microstructural refinement down to the optimal size of 0.1 to1.0 μm is necessary. The similar in-situ Mg-based BMGMC was also developed previously by Li *et al*. [5], but the microstructural length scale of their composite was much larger (~40 μm) compared to the optimal one. In the present work the microstructure of the BMGMC was adjusted to $L \approx S \approx R_p$ by controlling the in-situ formation process of α-Ti.

For inducing the in-situ formation of α-Ti in the Mg-Cu-Gd, the alloy was prepared by two-step procedures designed based on the enthalpy of mixing ($\Delta H^{mix}_{\{AB\}}$) which reflects the chemical interaction among atoms. In the first step, by pre-alloying Cu, Gd and Ti by arc-melting method, one can expect the formation of Ti-Cu and Gd-Cu phases because of the negative enthalpy of mixing for Ti-Cu and Gd-Cu and the positive one for Ti-Gd [7]. The result of the cross sectional analysis of the pre-alloyed ingot shows that the acicular and circular precipitates of Ti_2Cu were surrounded by Cu_7Gd_2 and Cu_2Gd (at.%), which is in good accordance with our prediction [8]. The second step is preparing the mother alloy by mixing the pre-alloy with pure Mg. In this step, the in-situ formation of pure Ti from the Ti-Cu phase is expected due to the negative enthalpy of mixing of Mg-Cu and Mg-Gd and the positive one for Mg-Ti [7]. Fig. 1 shows the SEM image and the corresponding elemental mapping of the cross section of the mother alloy [8]. Cu element (yellow) was not observed in the Ti rich area (green), but in the same areas (red) as the Mg rich matrix. This clearly confirms that Cu separated from the Ti_2Cu precipitates observed in the pre-alloy to form the Mg-Cu-Gd matrix with α-Ti dispersoids. An Mg-Cu-Gd BMGMC with in-situ α-Ti precipitates was then successfully formed by casting the mother alloy into a Cu-mold. The XRD pattern of the as-cast sample confirms the weak peaks of the α-Ti phase in

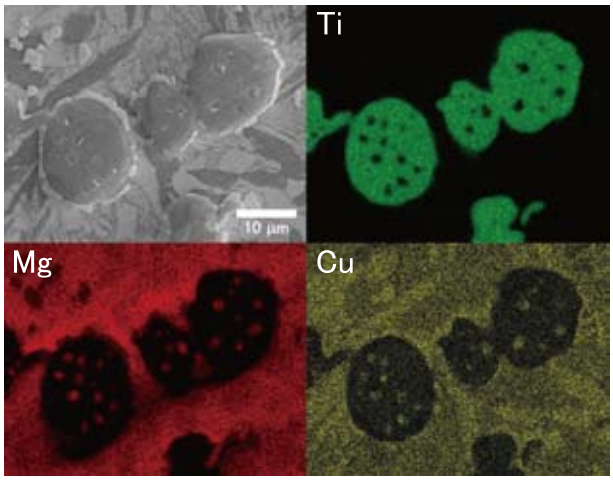

Fig. 1: SEM image and corresponding elemental maps of the mother alloy using slow-cooled prealloy for Ti (green), Mg (red) and Cu (yellow).

addition to the typical broad peak of the glassy structure.

It was also observed that the α-Ti dispersed in the glass matrix of the Mg-Cu-Gd BMGMC has porous plate-like structure and the size well corresponds to the plate-like Ti_2Cu in the pre-alloy. Accordingly, microstructural control of the pre-alloy may lead to the formation of finer Ti_2Cu, which in turn results in the in-situ formation of finer α-Ti dispersoids in the BMGMC. We then employed arc-melt type mold casting method during pre-alloying which enables the pre-alloy ingot to solidify at a much faster cooling rate. (Hereafter, the pre-alloy prepared by arc-melt type mold casting is called as rapidly-cooled (RC) pre-alloy, while that produced by slow solidification on a the copper hearth is called as slow-cooled (SC) pre-alloy).

Fig. 2 shows SEM image of an α-Ti dispersoid of the BMGMC prepared from the RC pre-alloy after the immersion in aqueous HNO_3. The dipersoid has a porous plate-like structure with a pore-size of ~500 nm, width of ~4 μm and thickness of ~500 nm [8]. It was much finer than that of the BMGMC prepared from the SC pre-alloy. The effective design for improving the toughness of the BMGMC was partially achieved, i.e. by controlling $L \approx R_p$.

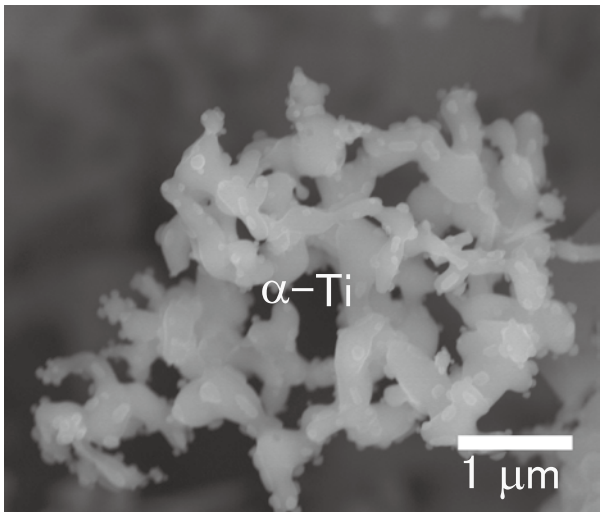

Fig. 2: α-Ti dispersoids obtained from the BMGMC made using the RC prealloy filtered after immersion in aqueous HNO_3.

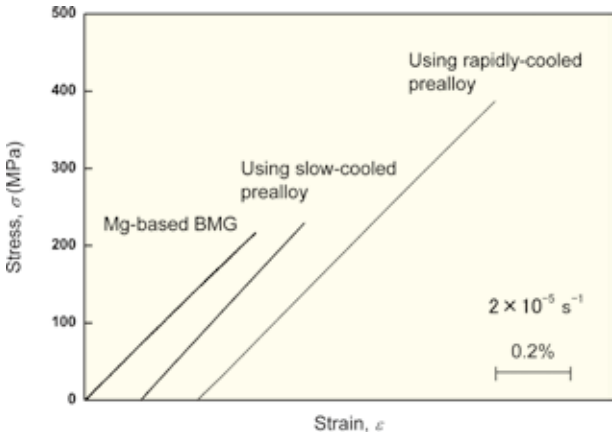

Fig. 3: Stress-Strain curves of the BMGMCs prepared using rapidly-cooled prealloy (RC prealloy) and slow-cooled prealloy (SC pre-alloy) under the four-point bending test. The curve of the monolithic $Mg_{61}Cu_{28}Gd_{11}$. BMG is inserted for comparison.

The size-refinement of the porous α-Ti in the BMGMC results in the increase of the maximum fracture stress under the four-point bending mode from 230 MPa (the SC pre-alloy BMGMC) to 387 MPa (the RC pre-alloy BMGMC) as shown in Fig. 3. Moreover, the localized plastic deformation via continuous slips of multiple shear bands was also observed in the tensile side surface [8].

References

[1] M.F. Ashby, A.L. Greer., *Scripta. Mater.* **54**, 321 (2006).
[2] J.S.-C. Jang, S.-R. Jian, T.-H. Li, J.C. Huang, C.Y.-A. Tsao and C.-T. Liu., *J. Alloys Compd.* **485**, 290 (2009).
[3] M. Kinaka, H. Kato, M. Hasegawa, A. Inoue., *Mater. Sci. Eng. A.* **494**, 299 (2008).
[4] H. Ma, J. Xu and E. Ma., *Appl. Phys. Lett.* **83**, 2793 (2003).
[5] F. Li, S. Guan, B. Shen, A. Makino and A. Inoue., *Mater. Trans., JIM* **48**, 3193 (2007).
[6] D.C. Hofmann, J-Y. Suh, A. Wiest, G. Duan, M-L. Lind, M.D. Demetriou and W.L. Johnson., *Nature* **451**, 1085 (2008).
[7] A. Takeuchi, A. Inoue., *Mater. Trans., JIM* **46**, 2817 (2005).
[8] H. Oka, T. Wada, A. Inoue and H. Kato., *J. Mater. Res . under review.*

Keywords: composite, mechanical properties, metallic glass
Hideki Oka (Non-Equilibrium Materials)
E-mail: hideki-o@imr.tohoku.ac.jp
Category: Energy-related Materials

Growth Mechanism of Si-faceted Dendrites

The growth mechanism of faceted dendrites has not been clarified since the discovery of the faceted dendrite of germanium in the 1950s. We successfully observed the growth processes of Si-faceted dendrites by *in situ* observation technique. The growth model of the faceted dendrites is established based on our experimental results.

Dendrites of faceted materials, so-called 'faceted dendrites', which are distinguished from the dendrites of nonfaceted materials in metals and alloys, were discovered in the 1950s [1]. Recently, Si-faceted dendrites have attracted much attention from both scientific and technological viewpoints due to their unique crystal structures. The surface of the faceted dendrite is bounded by {111} habit planes, and at least two parallel twins exist at the center of the faceted dendrite. It is also known that the preferential growth direction of faceted dendrites is <112> or <110>. Such features can be applied in technologies for growing thin Si ribbon crystals and polycrystalline Si ingots for solar cells.

The growth model of faceted dendrites preferentially grown in the <112> direction, hereafter referred to as <112> dendrites, was first proposed in 1960 by Hamilton and Seidensticker [2]. The model had been widely accepted although the actual growth behavior had remained mystery because of the lack of direct evidence. We recently succeeded in observing the growth behavior of <112> dendrites by *in situ* observations, and proposed a growth model based on experimental results of the growth behaviors of <112> dendrites [3]. On the other hand, no growth model of <110> dendrite has been proposed.

We succeeded in directly observing the growth processes of <110> dendrites by using an *in situ* observation system, which consisted of a furnace and a microscope [4].

Fig. 1(a) shows a <110> dendrite and a <112> dendrite growing from a part of a faceted crystal-melt interface. The shape of the tip of the growing dendrite is markedly different between the <110> and <112> dendrites. Although the tip of the <112> dendrite becomes wider during growth, that of the <110> dendrite remains narrow during growth.

We presented a growth model of <110> dendrites based on our experimental evidence, as shown in Fig. 1(b). The first illustration in Fig. 1(b) shows the equilibrium form of the Si crystal with two parallel {111} twin boundaries. The crystal is bounded by {111} habit planes. It is found that reentrant corners with an external angle of 141° (type Ⅰ) exist at both twins. Rapid growth occurs at these type Ⅰ corners, and leads to the formation of triangular corners. Although the rapid growth is inhibited after the formation of triangular corners, the crystal continuously grows on the {111} flat surface. When the triangular crystals propagated across the other twin, two type Ⅰ corners appear, and rapid growth occurs there again. The later growth processes are the same as described before. Note that the tip of the dendrite remains narrow during dendrite growth. Thus, we can explain the shape of the <110> dendrite during growth, shown in Fig. 1(a), by this mechanism.

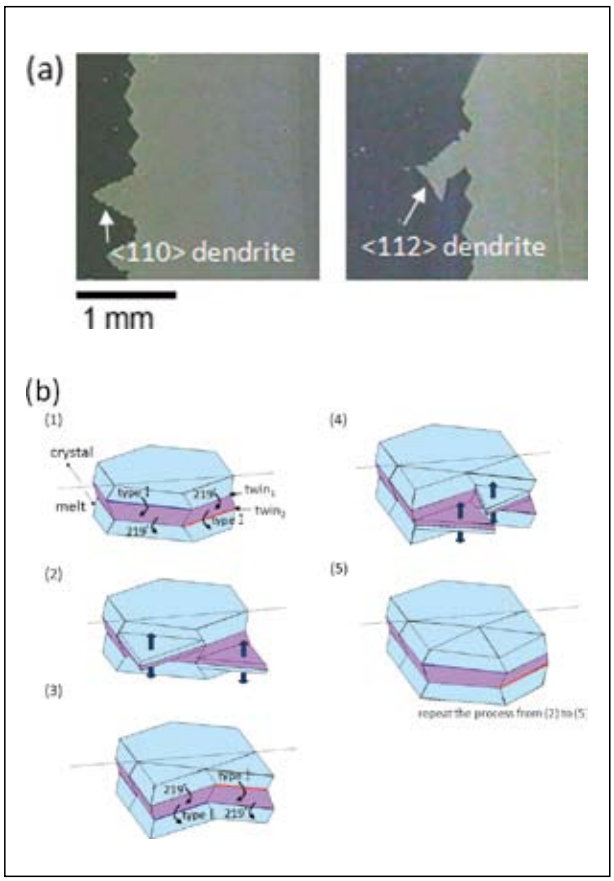

Fig. 1: (a) Growth shape of Si <110> and <112> dendrites. (b) Growth model of the <110> dendrite [4].

We have developed an equation for the theoretical growth velocity of a Si <110> faceted dendrite on the basis of the growth model shown in Fig. 1(b) [5]. The theoretical growth velocity is described as

$$V_{<110>}=\frac{h}{\sqrt{3}(h/V_1+d/V_2)}+V_2\,, \quad (1)$$

where *h* is the height of the triangular corner, *d* is the twin spacing, V_1 is the growth velocity at a type Ⅰ corner, and V_2 is the growth velocity on the {111} plane. It is found that the growth velocity of the dendrite is inversely proportional to twin spacing.

Fig. 2 (a) shows the growth of three dendrites (d1, d2, d3) from the same crystal-melt interface at the same time. The preferential growth direction of these three dendrites is <110>. It is found that the growth velocities are obviously different among the three dendrites. Fig. 2(b) shows the parallel twins observed at the center of d1, d2, and d3 by EBSP measurement. The average twin spacings in d1, d2, and d3 are 4.5 μm, 10 μm, and 16.5 μm, respectively. Dendrite growth velocity as a function of twin spacing is plotted in Fig. 2 (c). As twin spacing decreases, dendrite growth velocity nonlinearly increases. We use Eq. (1) to fit the experimental results, as shown by the red line in Fig. 2(c). Equation (1) fits quite well with the experimental results. The fitting results of *h*, V_1, and V_2 are 45±5 μm, 4600±500 μm/s, and 120±5 μm/s, respectively. It is found that the growth velocity at the type Ⅰ corner is much faster than that on {111} plane. It is also found that the growth velocity of a dendrite eventually approaches a certain value as twin spacing increases to infinity.

We also investigated the dependence of the growth velocity of faceted dendrites on undercooling [6]. The growth velocity increased linearly with increasing undercooling. We found that the relationship between the growth velocity and undercooling is most sensitive to twin spacing.

In summary, we investigated the growth mechanism of Si-faceted dendrites. The growth model of the Si-faceted dendrite was established based on the experimental results by *in situ* observations. Our *in situ* observation technique is a powerful tool for revealing the crystal growth mechanism.

References

[1] E. Billig, *Proc. R. Soc. London* Ser. A **229** (1955) 346.
[2] D. R. Hamilton and R. G. Seidensticker, *J. Appl. Phys.* **31** (1960) 1165.
[3] K. Fujiwara *et al.*, *Phys. Rev. Lett.* **101** (2008) 055503.
[4] K. Fujiwara *et al.*, *Phys. Rev. B* **81** (2010) 224106.
[5] X. Yang *et al.*, *Appl. Phys. Lett.* **97** (2010) 172104.
[6] X. Yang *et al.*, *Appl. Phys. Lett.* **98** (2011) 012113.

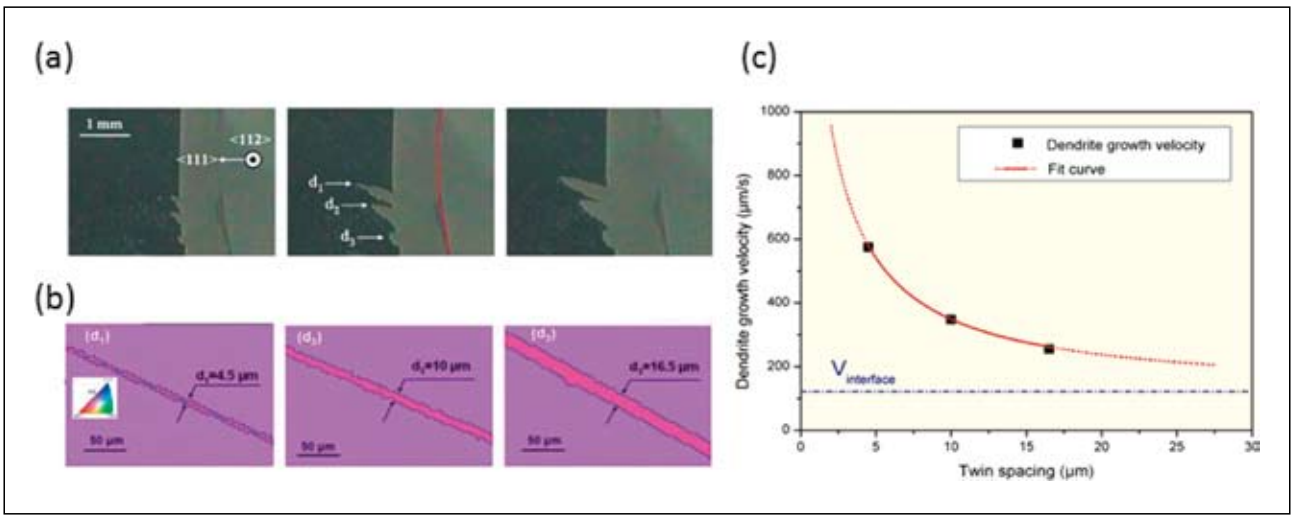

Fig. 2: (a) Growth behavior of faceted dendrites. Three dendrites grew from the same crystal-melt interface [5]. (b) Parallel twins observed at the center of the three dendrites [5]. (c)Dendrite growth velocity as a function of twin spacing [5].

Keywords: crystal growth
K. Fujiwara (Crystal Chemistry Division)
E-mail: kozo@imr.tohoku.ac.jp
URL:http://www.uda-lab.imr.tohoku.ac.jp

High-speed Preparation of YBCO Superconducting Film by Laser Chemical Vapor Deposition

In high-temperature superconducting wire, superconducting layer ($YBa_2Cu_3O_{7-\delta}$; YBCO) has generally been prepared by pulsed laser deposition or chemical vapor deposition (CVD). However, their low deposition rate and low yield constant are issues in practical production process. Chemical composition and orientation of the superconducting layer should also be precisely controlled in order to archive a high superconducting performance. We have developed a new laser CVD and successfully prepared *a*-axis oriented CeO_2 film for buffer layer and *c*-axis oriented YBCO film for superconducting layer on multilayer-coated Hastelloy tape substrate at high deposition rate.

High-temperature superconducting (HTS) materials having a critical temperature (T_C) above 77 K (boiling point of liquid nitrogen) opens up a new horizon for applying superconductivity to electrical devices. One of the most promising HTS materials is $YBa_2Cu_3O_{7-\delta}$ (YBCO). The T_C of YBCO is approximately 90 K and its high critical current density (typically over 1 MA/cm^2) is the best to use for power devices.

In HTS practical application including power cables, generators, motors and sensing devices, a flexible superconducting wire with a long length up to several kilometers is required. In order to meet this requirement, Ni-Cr alloy (Hastelly® C-276) tape is used as a substrate. On the tape substrate, oxide buffer layers, such as $Gd_2Zr_2O_7$, MgO, $LaMnO_3$ and CeO_2 are generally deposited by physical vapor deposition. These buffer layers can prevent the oxidization of the metal substrate at high temperature, reduce lattice mismatches and the thermal coefficient mismatches between YBCO superconducting layer and tape substrate, and provide an in-plane epitaxial growth of *c*-axis oriented YBCO layer.

Various deposition techniques, such as sol-gel, metalorganic deposition using trifluoroacetates (TFA-MOD), pulsed laser deposition (PLD), sputtering, thermal evaporation, molecular beam evaporation (MBE) and metalorganic chemical vapor deposition (MOCVD) has been employed for preparation of CeO_2 buffer layer and YBCO superconducting layers. Main issues for above techniques are relatively low deposition rates (below 1 μm/h). In practical application, high speed preparation of YBCO and CeO_2 films is required.

We have developed new coating Laser chemical vapor deposition (laser CVD) [1,2], which could be an effective approach to prepare highly oriented YBCO film and its buffer layer CeO_2 film at high deposition rate.

Preparation of CeO_2 film

a-axis oriented CeO_2 films epitaxially grown on (100) $SrTiO_3$ single crystal substrate at the whole laser power from 52 to 182 W (deposition temperatures of 952–1119 K). As for the (100) CeO_2 films on (100) $SrTiO_3$ substrate, their XRD pole figure patterns showed fourfold reflections at α = 45°, attributing to the {220} planes. The pole figure pattern from $SrTiO_3$ (110) showed a fourfold reflection at α = 45°, attributing to the {110} planes. The azimuth angle β of the four pole peaks from the CeO_2 film showed a 45° rotation on the basal plane of $SrTiO_3$ substrate, implying the in-plane epitaxy of (100) CeO_2 // (100) $SrTiO_3$ and CeO_2 [010] // $SrTiO_3$ [011].

Microstructure of (100) CeO_2 films prepared on (100) $SrTiO_3$ substrate consisted of rectangular-shaped grains (Fig. 1(a)) and showed a columnar growth in the cross section.

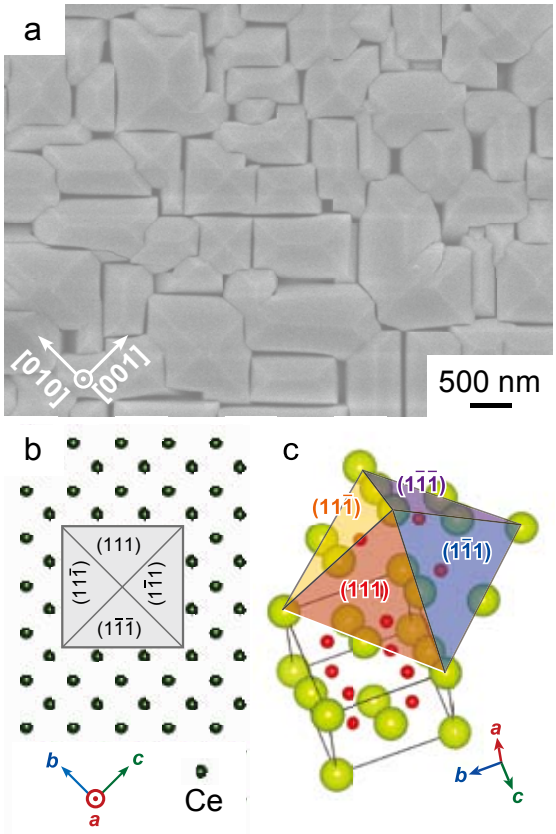

Fig. 1: (a) Surface microstructure, (b) schematic of in-plane orientation and (c) atomic arrangement of CeO_2 film prepared on (100) $SrTiO_3$ substrate by laser CVD.

The pyramidal caps of the rectangular-shaped grains were attributed to CeO_2 {111} planes (Fig. 1(b)). The {111} planes had lowest surface energy (9.6 eV/nm^2) among the low index planes of (110), (211), (100), (210) and (310) which had surface energy of 15.3, 16.7, 20.3, 20.4 and 22.4 eV/nm^2, respectively. CeO_2 {111} planes were therefore energetically favorable to be formed at the late deposition stage of CeO_2 film.

Preparation of YBCO film

Fig. 2(a) shows the YBCO films prepared on multilayered Hastelloy C-276 tape with (100) CeO_2 top layer. *c*-axis oriented YBCO film was epitaxially grown on (100) CeO_2 top layer (Fig. 2(b)). The electrical resistivity of *c*-axis-oriented YBCO films decreased linearly with lowering the temperature in normal state and showed sharp zero resistance transitions at T_C = 90 K (Fig. 2(c)).

The XRD pole figure from the (102) reflection of the *c*-axis-oriented YBCO film showed a fourfold pattern at around α = 33°, which was attributed to {102} planes with the complementary angle of 57° to the (001) plane (Fig. 2(d)). The azimuth angles β of the pole peaks from (102) reflection of the c-axis-oriented YBCO film rotated 45° with respect to those of CeO_2 (220) reflection (Fig. 2(d)), indicating the in-plane alignment growth of YBCO (001) // CeO_2 (100) and YBCO [100] // CeO_2 [011] (Fig. 2(e)). *a*-axis- and *c*-axis-oriented YBCO films were also obtained by changing laser power. The preferred orientation changed from *a*-axis to *c*-axis with increasing laser power.

The deposition rate of *c*-axis oriented YBCO films was 83 μm/h, and this was about 3-900 times higher than that of YBCO by conventional MOCVD [3].

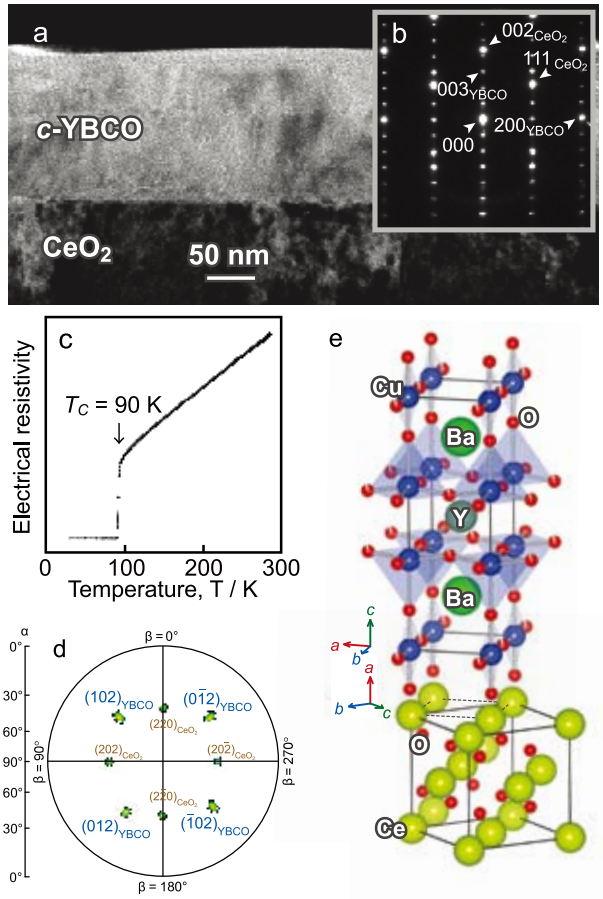

Fig. 2: (a) Cross-sectional microstructure of c-axis oriented YBCO film prepared on (100) CeO_2 top layer of multilayer-coated Hastelloy tape, (b) selected area electron diffraction patterns, (c) electrical resistivity against temperature, (d) pole figure patterns and (e) atomic arrangement of YBCO film on CeO_2 (100). TEM observation courtesy of JFCC.

References

[1] T. Goto *et al.*, *Thin Solid Films* **515** (2006) 46.
[2] A. Ito *et al.*, *J. Alloys Compd.* **489** (2010) 469.
[3] P. Zhao *et al.*, *Supercond. Sci. Technol.* **23** (2010) 125010.

Keywords: chemical vapor deposition, ceramic, superconducting
T. Goto, R. Tu and A. Ito (Multi-Functional Materials Science Division)
E-mail: goto@imr.tohoku.ac.jp
URL:http://www.goto.imr.tohoku.ac.jp/

Production of Ni-Cr-P-B Alloy-Coated Bipolar Plates for PEMFC by HVOF Spray-Coating and Their Surface Analysis by XPS

In this study, the newly designed bipolar plates for proton exchange membrane fuel cells (PEMFC) were produced by the High Velocity Oxy-Fuel(HVOF) spray-coating the $Ni_{65}Cr_{15}P_{16}B_4$, $Ni_{60}Cr_{20}P_{16}B_4$ and $Ni_{55}Cr_{25}P_{16}B_4$ alloys on Al plates having a flow field. The I-V performance of a single fuel cell with these bipolar plates produced in this work was studied and we found that the single fuel cells with the alloy-coated bipolar plates showed high I-V performance as well as the cell with the carbon bipolar plates. After that, the 24h durability tests were conducted. As the result, the cell voltage of a single fuel cell with the alloy-coated bipolar plates did not show significant voltage drop during the tests. Furthermore, XPS analysis of the surface layer of the Ni-Cr-P-B alloy-coated bipolar plates was conducted after the 24h durability tests. It was found that the surface passive film of Ni-Cr-P-B alloy contains the Cr_2O_3 of very high concentration, resulting in high I-V performance and good durability.

Bipolar plates are one of the most important components of PEM fuel cells and are multifunctional as they conduct electricity from cell to cell, they separate the fuel gas from the oxidant gas, and their flow field supplies the gases to the electrodes. Bipolar plates are conventionally made of carbon graphite. However, high production cost of graphite bipolar plate inhibits wide spread use of the fuel cells. Moreover, it cannot be used to make a thinner bipolar plate because of its significant brittleness.

Compared to the carbon graphite, the metallic materials have many advantages such as low-cost, good electrical and thermal conductivities, excellent mecha- nical properties and good workability. However, corrosion may occur when the metallic bipolar plates are used under acidic atmosphere in the fuel cells, which leads to the dissolution of metallic ions.

So, we focused on metallic glass which is known for its extremely high corrosion resistance and tentatively produced the Ni-Cr-P-B metallic glass-coated bipolar plates by using the High Velocity Oxy-Fuel (HVOF) spray coating technique in this study. The electricity generating properties of the single fuel cell with the metallic glass-coated bipolar plates were also examined [1,2]

Production of metallic glass-coated bipolar plates

The bipolar plates were produced by the HVOF spray-coating the $Ni_{65}Cr_{15}P_{16}B_4$, $Ni_{60}Cr_{20}P_{16}B_4$ and $Ni_{55}Cr_{25}P_{16}B_4$ alloys on Al plates having a flow field.

Fig. 1 shows the outer view of the $Ni_{60}Cr_{20}P_{16}B_4$ metallic glass-coated Al bipolar plate produced by HVOF spray-coating and subsequent hot-pressing. The glass film was deposited on both sides of the plates. As a result of XRD observations, it was found that the HVOF spray-coated $Ni_{65}Cr_{15}P_{16}B_4$ and $Ni_{60}Cr_{20}P_{16}B_4$ alloy films deposited on Al plates showed mainly a broad hallo peak coming from the glassy matrix and a small peaks from the crystalline phases. The spray-coated $Ni_{55}Cr_{25}P_{16}B_4$ alloy showed sharp distinct peaks coming from crystalline phases.

Power generation tests with metallic glass-coated bipolar plates

Fig. 2 shows the I-V performance of a single fuel cell with these bipolar plates produced in this work. It was found that the single fuel cells

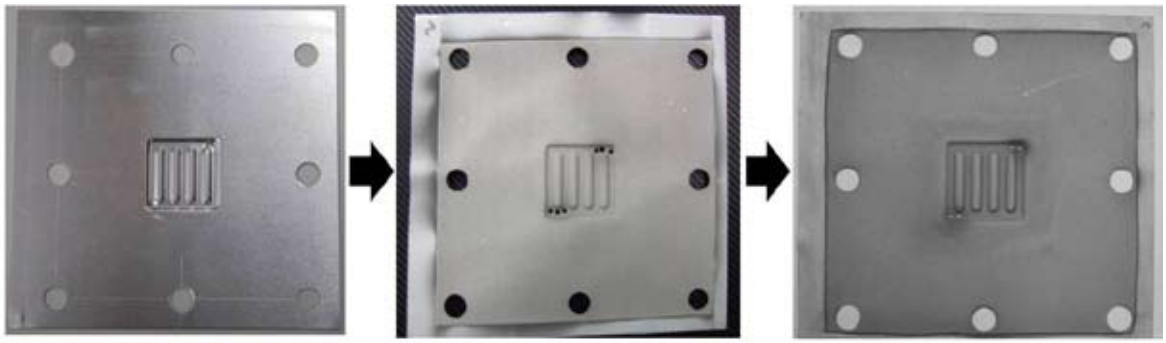

Fig. 1 : Schematic illustration of the flow field.

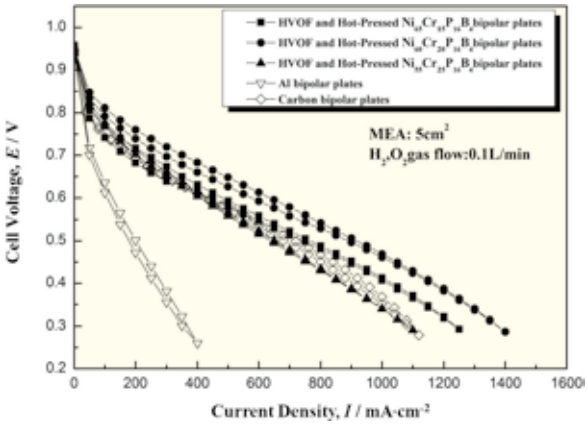

Fig. 2 : I-V curves measured with a single fuel cell with carbon, Al, $Ni_{65}Cr_{15}P_{16}B_4$[35], $Ni_{60}Cr_{20}P_{16}B_4$ and $Ni_{55}Cr_{25}P_{16}B_4$ alloy-coated bipolar plates measured after 50 cycles repetition.

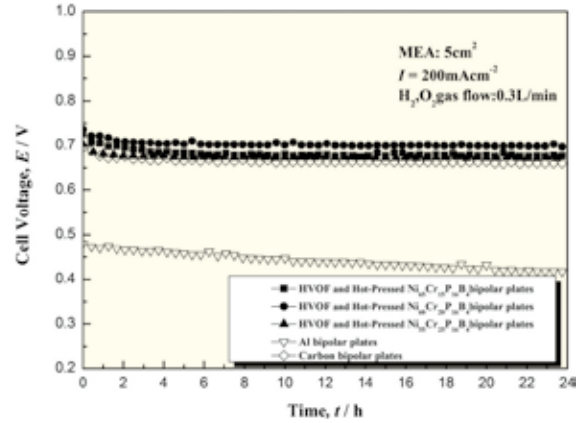

Fig. 3 : 24h durability tests conducted at a constant current density of 200 mA•cm^{-2} with a single fuel cell with carbon, Al, $Ni_{65}Cr_{15}P_{16}B_4$[35], $Ni_{60}Cr_{20}P_{16}B_4$ and $Ni_{55}Cr_{25}P_{16}B_4$ alloy-coated bipolar plates.

with the alloy-coated bipolar plates showed high I-V performance as well as the cell with the carbon bipolar plates. Among them, the $Ni_{60}Cr_{20}P_{16}B_4$ alloy showed the highest I-V performance, showing the largest current density at 0.3 V.

Fig. 3 shows the 24h durability tests conducted at the constant current density of 200 mA•cm^{-2}. The cell voltage of a single fuel cell with the alloy-coated bipolar plates did not show significant voltage drop during the tests. It can be concluded that the most suitable alloy in this study is $Ni_{60}Cr_{20}P_{16}B_4$ alloy.

XPS Analysis of metallic glass-coated bipolar plates

Fig. 4 shows the results of the XPS analysis of the surface layer of the Ni-Cr-P-B alloy-coated bipolar plates after the 24h durability tests. As a result, the Cr_2O_3 passive film was found in all the Ni-Cr-P-B alloy surface films and also the P_2O_5 in the $Ni_{65}Cr_{15}P_{16}B_4$ and $Ni_{55}Cr_{25}P_{16}B_4$ alloy surface films and $Ni(OH)_2$ in the $Ni_{65}Cr_{15}P_{16}B_4$ alloy surface film. This observation indicates that the surface passive film of $Ni_{60}Cr_{20}P_{16}B_4$ alloy contains the Cr_2O_3 of the highest concentration among the three alloy surface films, resulting in the highest I-V performance and good durability.

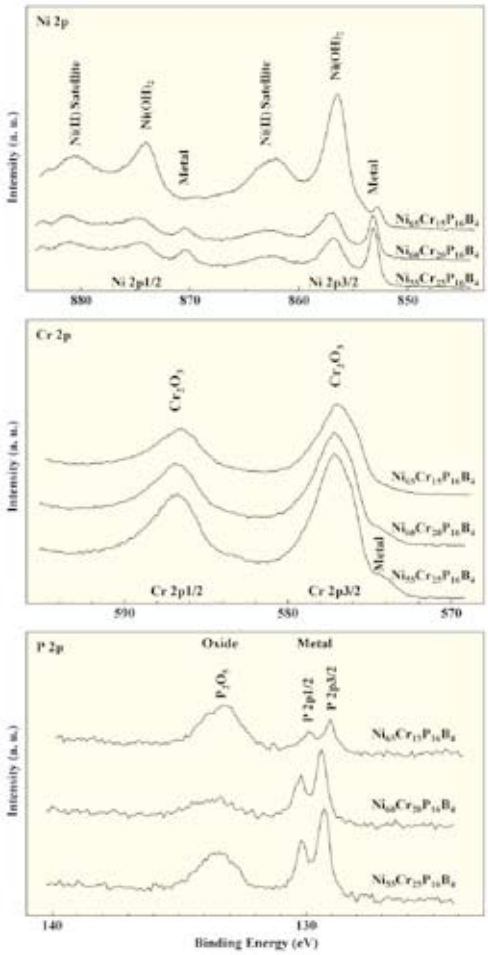

Fig. 4 : XPS Ni 2p, Cr 2p and P 2p narrow region scans of the $Ni_{65}Cr_{15}P_{16}B_4$, $Ni_{60}Cr_{20}P_{16}B_4$ and $Ni_{55}Cr_{25}P_{16}B_4$ alloy.

References

[1] S.C.Kim, S.Yamaura, Y.Shimizu, K.Nakashima, T.Igarashi, A.Makino and A.Inoue, Mater. Trans. **51**, 1609 (2010).

[2] S.C.Kim, *S.Yamaura, T.Igarashi, Y.Shimizu, K.Nakashima, A.Makino and A.Inoue, J. Japan Inst. Metals* ***75***, 122 (2011).

Keywords: fuel Cell, metallic glass, coating
S. Yamaura (Metallic Glass NEDO Laboratory)
E-mail: yamaura@imr.tohoku.ac.jp
URL: http://nedo-koza.imr.tohoku.ac.jp/

Point Defect Processes before Steady-state Void Growth in Austenitic Stainless Steels

Defect structures during the incubation period in austenitic stainless steels, both commercial alloys such as SUS316SS and model alloys such as Fe-Cr-Ni, were studied using positron annihilation lifetime measurements. By fission neutron irradiation to 0.2 dpa at 363 K, single vacancies were formed in the commercial alloys and large voids were formed in the model alloys. After irradiation at 573 K, stacking fault tetrahedra and/or precipitates were detected in the commercial alloys, while large voids were formed in the model alloys. Defect evolution during the incubation period was discussed on the basis of neutron irradiation results.

Nuclear materials are vulnerable to void swelling during prolonged neutron irradiation. Before swelling, there exists an incubation dose as shown in Fig. 1. After the dose, a steady state void swelling, 1%/dpa, starts in both model alloys and commercial alloys of austenitic stainless steels. The dose determines the duration of service under neutron irradiation in nuclear reactors. The start of void swelling strongly depends on alloying elements. In Ni, voids were observed by transmission electron microscopy (TEM) after fusion neutron irradiation of 10^{-3} dpa at 573 K [1]. Ni is the simplest model metal of austenitic stainless steels from the viewpoint of crystal structure and lattice constant. In a model alloy of austenitic stainless steels, Fe-Cr-Ni ternary alloy, voids were observed at a dose of 0.1 dpa at 573 K [2], and in a commercial alloy of Ti added modified SUS316SS, no voids were observed at a dose of 15 dpa at 701 K [3].

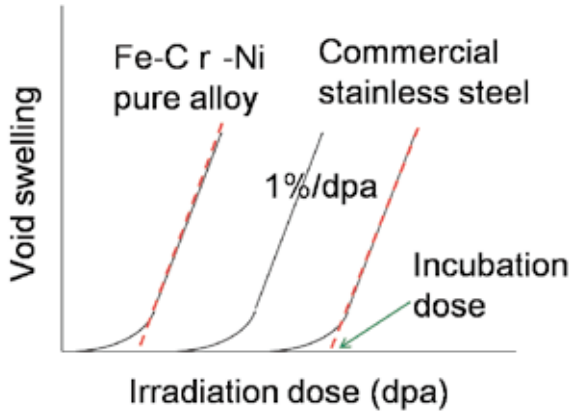

Fig. 1: Schematic illustration of incubation dose for void swelling in austenitic stainless steels.

As most experimental studies have been performed after void formation using TEM, point defects and their clusters smaller than the resolution limit were impossible to detect. Positron annihilation spectroscopy makes it possible to detect small defects, which are below the resolution limit of TEM. In this study, point defect processes occurring during the incubation period of austenitic stainless steels were studied using positron annihilation lifetime measurements.

Specimens used were 99.99 % pure Ni, four model alloys, specimen ID A: Fe-16.1Cr -17.0Ni, B: Fe-15.4Cr-15.9Ni-2.68Mo-1.89Mn, C: Fe-15.3Cr-15.8N-2.66Mo-1.88Mn-0.53Si and D: Fe-15.3Cr-15.8N-2.66Mo-1.88Mn-0.53Si-0.24Ti, and four commercial alloys, J: Ti added modified SUS316SS (Fe-15.27Cr-15.8Ni-2.66Mo-1.88Mn-0.53Si-0.24Ti-0.055C-0.024P), E: SUS316L SS, F: SUS316SS and G: SUS304SS. Positron annihilation lifetimes of the specimens were measured at room temperature using a conventional fast-fast spectrometer with a time resolution of 190 ps (full width at half maximum) and each spectrum was accumulated to a total of 1×10^6 counts. The positron lifetime spectra were analyzed using the PALSfit program [4] and the lifetimes were decomposed into two (τ_1, τ_2) or three components (τ_1, τ_2, τ_3) if possible. Otherwise only an average lifetime (τ_{av}) was obtained.

Positron annihilation lifetimes of Fe-14Cr-13Ni were almost the same as those of Ni [5-7] and we used the lifetime of Ni for the identification and the estimation of size of defect clusters such as voids and stacking fault tetrahedral in austenitic stainless steels. The lifetimes of them are as follows. Single vacancy: 176 ps, di-vacancies: 195 ps, voids of 79 vacancies: 427 ps, stacking fault tetrahedra of 21 vacancies: 155 ps, stacking fault tetrahedra of 28 vacancies: 130 ps.

Before neutron irradiation, the positron annihilation lifetimes were between 106 and 109 ps. After neutron irradiation using fission neutrons from BR-2 of SCK•CEN at 363 K and 573 K to a dose of 0.2 dpa, the lifetimes changed as shown in Tables 1 and 2. Dashes in these tables indicate that two- or three- component analysis of the positron annihilation lifetime spectra was impossible.

The long lifetime of positron annihilation depends on a size of vacant site where positrons were annihilated. The longer and shorter lifetime than that of single vacancies (176 ps [6]) suggests the existence of larger vacancy clusters (voids) and smaller spaces than single vacancies, respectively. Following 363 K

Table 1: Positron annihilation lifetimes of model alloys and commercial alloys of austenitic stainless steels irradiated at 363 K to 0.2 dpa.

ID	τ_{av}(ps)	τ_1(ps)	τ_2(ps)	I_2(%)
Ni	271±1	161±2	403±4	46±1
A	183±1	169±1	486±28	4±1
B	176±1	135±8	195±4	67±9
C	177±1	128±8	193±3	73±7
D	176±1	114±9	187±2	82±4
J	154±1	50±3	174±1	84±1
F	181±1	-	-	-
G	185±1	-	-	-

Table 2: Positron annihilation lifetimes of model alloys and commercial alloys of austenitic stainless steels irradiated at 573 K to 0.2 dpa.

ID	τ_{av}(ps)	τ_1(ps)	τ_2(ps)	I_2(%)	τ_3(ps)	I_3(%)
Ni	195±1	54±7	154±3	70±1	433±7	17±1
A	233±1	39±5	164±2	68±1	511±5	21±1
B	273±1	46±4	162±3	55±1	523±4	29±1
C	148±1	47±2	157±1	79±1	489±33	2±1
D	156±1	53±2	161±1	72±1	549±14	4±1
J	148±1	53±16	149±1	96±1	-	-
E	149±1	84±23	153±2	93±5	-	-
F	149±1	-	-	-	-	-
G	146±1	-	-	-	-	-

irradiation as listed in Table 1, the lifetimes of Ni, A, B, C, D and J were decomposed into two components. Large voids were formed in Ni and the ternary model alloy (A), and only single vacancies were detected in model alloys B, C, and D, and in the commercial alloys J, F and G.

At the 573 K irradiation, the mean lifetimes were lower than those at 363 K as listed in Table 2. The lifetime τ_3 of Ni and of the four model alloys indicated the formation of voids. The lifetimes in the commercial alloys were lower than those of single vacancies, and the lifetime corresponds to that of stacking fault tetrahedra [6] and grain boundaries. Therefore at low dose of 0.2 dpa, voids were not formed in the commercial alloys but other defects were formed.

As metal carbides which are commonly formed by irradiation of austenitic stainless steels have incoherent grain boundaries with the matrix, vacant spaces smaller than single vacancies were formed. By TEM observation, the formation of metal carbides in austenitic stainless steels was observed only at higher temperatures and higher irradiation doses than were used in the present experiment [8]. However, there is a strong possibility of the formation of very small precipitates at low temperatures and low doses, and these can be detected by positron annihilation lifetime measurements.

363 K neutron irradiation formed large voids in Ni and A, while only single vacancies and di-vacancies were formed in other alloys. Although voids were formed in Ni and A, the intensities I_2, which present the ratio of positrons annihilated at voids, indicated that the number of voids in A was very small compared to Ni. 573 K irradiation formed voids in Ni and the four model alloys. The intensity of long lifetimes τ_3 was, however, decreased with the addition of Si (C and D) and no voids were formed with the addition of C and/or P (E, F,G and J).

In all model alloys and commercial alloys, single vacancies can move at 573 K, and vacancy clusters, voids, are only formed in model alloys at 573 K even with the low dose of 0.2 dpa. Therefore, the formation of voids is prevented in the commercial alloys, and stacking fault tetrahedra and/or precipitates are formed instead. For the growth of voids in the commercial alloys at higher dose (above incubation dose), other factors such as purification of the matrix by irradiation (by irradiation induced segregation, for example) may be required, because voids are easily formed in the model alloys.

References

[1] S.Kojima, T.Yoshiie, M.Kiritani, J. Nucl. Mater. **155-157** (1988) 1249.

[2] M. Horiki, M. Kiritani, J. Nucl. Mater., **212-215** (1994) 246.

[3] T. Yoshiie, X.Z. Cao, K. Sato, K. Miyawaki, Q. Xu, J. Nucl. Mater., Accepted.

[4] P. Kirkegaard, J. V. Olsen, M. Eldrup, N. J. Pedersen, Risø DTU, February 2009, ISBN 978-87-550-3691-8, 44 p, http://palsfit.dk/ .

[5] B .L. Shivachev, T.Troev, T.Yoshiie, J. Nucl. Mater. **306** (2002) 105.

[6] E. Kuramoto, T. Tsutsumi, K. Ueno, M. Ohmura, Y. Kamimura, Comp. Mater. Sci., **14** (1999) 28.

[7] H. Ohkubo, Z. Tang, Y. Nagai, M. Hasagawa, Y. Tawara, M. Kiritani, Mater. Sci. Eng. A, **350** (2003) 92.

[8] T. Yoshiie, X. Cao, Q. Xu, K. Sato, T. D. Troev, Phys. Status Solidi C 6 (2009) 2333.

Keywords: radiation effects, neutron irradiation, nuclear materials
T.Yoshiie (Research Reactor Institute, Kyoto University)
E-mail:yoshiie@rri.kyoto-u.ac.jp
URL:http:// http://www.rri.kyoto-u.ac.jp/mre/

Development of New Nanocrystalline Soft Magnetic Materials Exhibiting ultra Low Electric Power Loss and High Magnetic Flux Density.

Fe-rich $Fe_{85-86}Si_{1-2}B_8P_4Cu_1$ nanocrystalline ribbons (~ 6 mm in width) made from industrial raw materials (containing some impurities) were developed. These ribbons exhibit high B of 1.82 - 1.85 T (at 800 A/m), almost comparable to commercial Fe- 3 mass% oriented Si alloy. Excellent magnetic softness (low $\boldsymbol{H}_c$ of 2.6-5.8 A/m, high permeability of 2.4-2.7x10^4 at 1 kHz and small saturation magnetostriction of 2.3-2.4x10^{-6}) along with high electrical resistivity (0.67-0.74 μΩm) of these alloys resulted in superior frequency characteristics of magnetic core losses (***W***) and a much lower ***W*** at 50 Hz up to the maximum induction of 1.75 T, in comparison to the silicon steels now in practical use for power applications.

For power applications such as transformers and motors, non-oriented silicon steel and oriented silicon steel are still now mainly used because of their high ***B***, despite of their much inferior magnetic softness. Magnetic core loss (***W***) in silicon steels have been improved for a long time, which recently seems to reach the limitation [1, 2]. Continued growth in electrical power generation and the recent energy problems strongly require decreasing wasteful dissipation of energy. Making efforts to reduce CO_2 emissions and conserve resources has come into an issue of global importance, and even among the electronic components industry consideration of the environment is a subject that cannot be ignored. Electrical power loss resulting from ***W*** in motors and transformers is estimated to be about 3.4% of the total domestic electrical power consumption in Japan[3]. Besides, in view of increasing demands of high efficiency and high performance electric motors for hybrid/electrical-vehicles (HEV/EV), reduction of tremendous amount of ***W*** in many kinds of motors and transformers requires development of new soft magnetic materials with high saturation magnetic flux density ($\boldsymbol{B}_s$) combined with low ***W***.

We have developed a new $Fe_{85-86}Si_{1-2}B_8P_4Cu_1$ nano-crystalline soft magnetic material composed of ~95 mass% Fe without rare-earth metals [4]. The new low-cost soft magnetic material exhibits high magnetic flux density (1.8 ~ 1.9 T) along with extremely low core-losses (1/2 ~ 1/3 of the ordinary materials). Fig. 1(a) shows the photograph of as-quenched $Fe_{83.3}Si_4B_8P_4Cu_{0.7}$ alloy ribbon (width - 50 mm and thickness ~ 23 μm). The wide ribbons can be easily melt-spun in air due to its lower melting temperature and its substantial resistance to oxidation. Nearly 6-mm-wide and ~ 20-μm-thick ribbons can be easily obtained for Fe-rich $Fe_{85}Si_2B_8P_4Cu_1$ alloy. The as-quenched ribbons show a complete ductility which should be a great advantage as an industrial material. Transmission electron microscopy showed a large number of extremely small a-Fe clusters (~3 nm) embedded in an amorphous materix, i.e. a hetroamorphous for as quenched ribbons [Fig. 1(b)]. An unusual uniform nanocrystalline structure composed of a-Fe grains with 10 - 20 nm in size [Fig. 1(c)] accompanied with an intergranular amorphous phase with ~1 nm in width was obtained on annealing at 460°C.

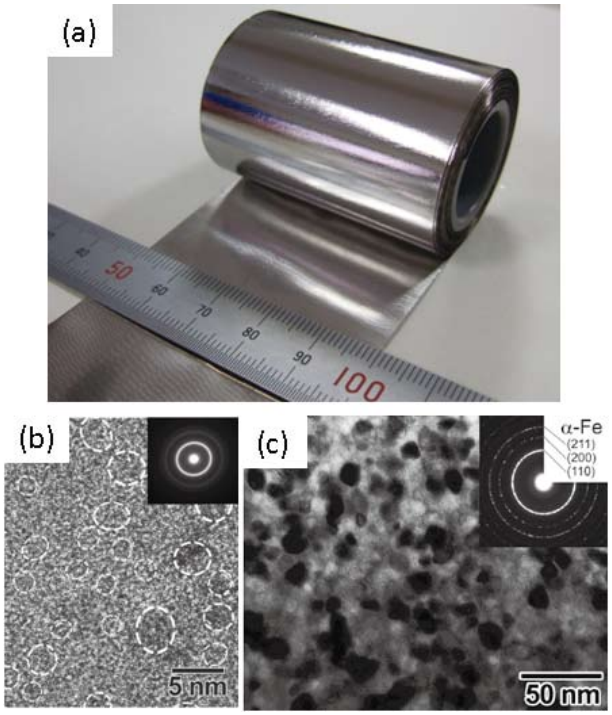

Fig. 1: (a) Outer appearance of the as-quenched $Fe_{85}Si_2B_8P_4Cu_1$ alloy ribbon with width of 6 mm and thickness of about 20 μm. Bright field TEM images with selected area electron diffraction patterns for the (b) as-quenched alloy ribbons , and (c) ribbon annealed at 460°C.

Fig. 2 shows the changes in physical and magnetic properties ($\boldsymbol{B}_{800}$, $\boldsymbol{H}_c$, $\boldsymbol{\rho}$ and ***R***) as a function of annealing temperature for the $Fe_{85}Si_2B_8P_4Cu_1$ alloy. $\boldsymbol{\rho}$ and ***R*** exhibit a drastic change with the precipitation of a-Fe in the

amorphous matrix. B_{800} increases from 1.13 T to 1.82 T with the structural change. Here it is noteworthy that high B_{800} and low H_c are exhibited on the crystallized $Fe_{85}Si_2B_8P_4Cu_1$ alloy, simultaneously.

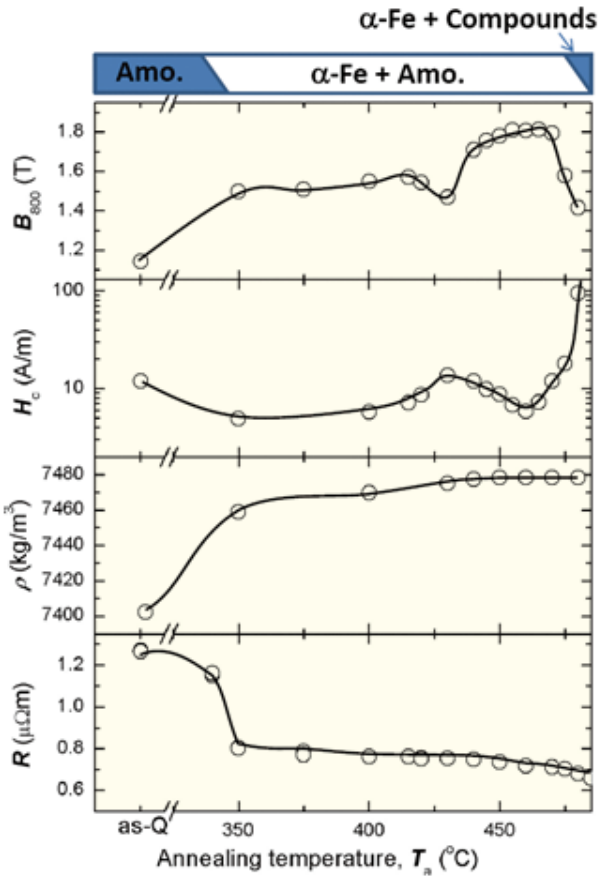

Fig.2: Annealing temperature dependence of magnetic flux density (B_{800}), coercivity (H_c), density (ρ) and resistivity (R) for the melt-spun $Fe_{85}Si_2B_8P_4Cu_1$ alloy. Structural change with annealing is also shown for comparison.

Fig. 3 shows the changes in magnetic core loss (W) at 50 Hz for the $Fe_{85-86}Si_{1-2}B_8P_4Cu_1$ nanocrystalline alloys as a function of maximum magnetic induction (B_m). The data of $Fe_{78}Si_9B_{13}$ amorphous, highest grade oriented Fe-3 mass% Si and non-oriented Fe-3 mass% Si and Fe-6.5 mass% Si alloys are also shown for comparison. W is a very important characteristic for the materials in power applications such as transformers and motors. The amorphous alloy with very low H_c of 2.6 A/m exhibits a very low W in the lower B_m range than around 1.2 T, and shows a rapid increase of W with further increasing B_m due to the magnetic saturation. The nanocrystalline alloys show significantly smaller W than all the silicon steels over the whole B_m range. Here, the very low W of the nanocrystalline alloy in the B_m range of 1.5 - 1.75 T is 1/2-1/3 smaller than that of the oriented Fe-3 mass% Si alloy, and overwhelmingly smaller than those of the non-oriented Fe-3 mass %Si and Fe-6.5 mass% Si alloys, which is important for the power applications. Additionally, $Fe_{85}Si_2B_8P_4Cu_1$ nanocrystalline alloy exhibit superior frequency characteristics of W comparable to the typical amorphous alloy and high T_c comparable to Fe-3 mass% Si alloys, higher R than Fe-3 mass% Si alloys and larger ε_f than the ordinary nanocrystalline and the amorphous alloys. It should be noted that these outstanding feature never seen in other soft magnetic materials.

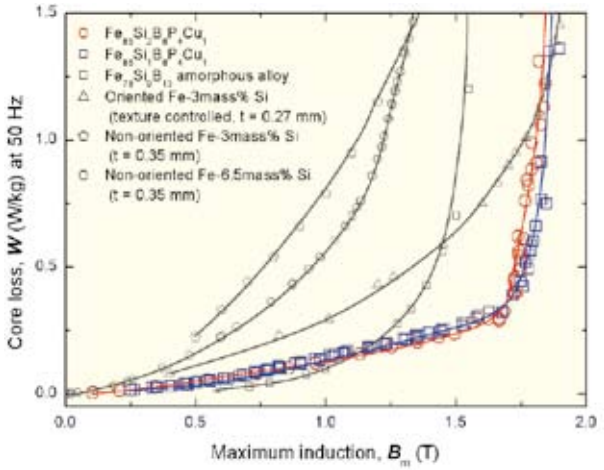

Fig.3: Magnetic core losses (W) of nanocrystallized FeSiBPCu alloys as a function of maximum magnetic induction (B_m). The data of $Fe_{78}Si_9B_{13}$ amorphous and Fe-Si crystalline alloys are also shown for comparison shown.

References

[1] Japan Iron and Steel Federation, Bulletin of Nishiyama Memorial Lecture, **155-156**, (1995) 111-149.
[2] Nippon Steel Company Co. LTD, Nippon Steel Monthly **141**, (2004).
[3] JFE 21 Century Foundation, [Online]. Available: http://www.jfe-21st-cf.or.jp/chapter_1/1d_2.html.
[4] A. Makino et al., J. Appl. Phys. **109** (2011) 07A302.

Keywords: nanocrystalline, soft magnetic, extremely low magnetic core losses
Akihiro Makino (Advanced Research Center of Metallic Glasses)
E-mail: amakino@imr.tohoku.ac.jp
URL: http://www.arcmg.imr.tohoku.ac.jp/